Attractive interaction and bridging transition between neutral colloidal particles due to preferential adsorption in a near-critical binary mixture

Ryuichi Okamoto[1] and Akira Onuki[2]
[1]*Fukui Institute for Fundamental Chemistry, Kyoto University, Kyoto 606-8103, Japan*
[2]*Department of Physics, Kyoto University, Kyoto 606-8502, Japan*
(Received 1 July 2013; published 19 August 2013)

We examine the solvent-mediated interaction between two neutral colloidal particles due to preferential adsorption in a near-critical binary mixture. We take into account the renormalization effect due to the critical fluctuations using the recent local functional theory [J. Chem. Phys. **136**, 114704 (2012)]. We calculate the free energy and the force between two colloidal particles as functions of the temperature T, the composition far from the colloidal particles c_∞, and the colloid separation ℓ. The interaction is much enhanced when the component favored by the colloid surfaces is poor in the reservoir. For such off-critical compositions, we find a surface of a first-order bridging transition $\ell = \ell_{cx}(T, c_\infty)$ in the T-c_∞-ℓ space in a universal, scaled form, across which a discontinuous change occurs between separated and bridged states. This surface starts from the bulk coexistence surface (CX) and ends at a bridging critical line where ℓ is determined by T as $\ell = \ell_c(T)$. On approaching the critical line, the discontinuity vanishes and the derivatives of the force with respect to T and ℓ both diverge. Furthermore, bridged states continuously change into separated states if c_∞ (or T) is varied from a value on CX to a value far from CX with ℓ kept smaller than $\ell_c(T)$.

DOI: 10.1103/PhysRevE.88.022309 PACS number(s): 64.70.pv, 68.35.Rh, 05.70.Jk, 64.75.Xc

I. INTRODUCTION

Much attention has been paid to the physics of fluids in restricted geometries [1,2]. The microscopic interactions between the fluid molecules and the solid surface can greatly influence the phase transition behavior of the confined fluid [3]. The liquid phase is usually favored by the walls in fluids undergoing gas-liquid phase separation, while one component is preferentially attracted to the walls in binary mixtures. In the film geometry, narrow regions may be filled with the phase favored by the confining walls or may hold some fraction of the disfavored phase. Between these two states, there can be a first-order phase transition, called capillary condensation [1,2,4], depending on the temperature T, and the reservoir chemical potential μ_∞ for each given wall separation D. This phenomenon occurs both in one-component fluids and in binary mixtures.

As another aspect, adsorption-induced density or composition disturbances are known to produce an attractive interaction between large particles [5,6]. In binary mixtures, it is amplified when the solvent far from these objects is poor in the component favored by the surfaces [6]. Such solvent-mediate interactions should play an important role in reversible aggregation of colloidal particles in near-critical binary mixtures [7–10], which has been observed between an aggregation curve and the bulk coexistence curve in the temperature-composition phase diagram. A number of theoretical papers treated the solvent-mediated colloid interaction and the resultant colloid aggregation [11–15]. It is worth noting that the observed aggregation curve closely resembles the precipitation curve due to highly selective impurities in a binary mixture [16]. Recently the colloid-wall interaction has been measured directly in a near-critical fluid [17,18].

In real colloids, other interactions are also relevant. First, we should account for the van der Waals (dispersion) interaction, which sometimes gives rise to intriguing effects in wetting behavior [3,4,19,20]. Dantchev *et al*. [21] examined the role of the van der Waals interaction in the film geometry near the bulk criticality on the critical path ($\mu_\infty = 0$ and $\tau > 0$). Second, in aqueous fluids, the colloid surfaces can be ionized so that the counterions and added ions form an electric double layer on each particle, resulting in the screened Coulomb interaction [3,4,19]. This repulsive interaction can be very strong close to the surfaces, but it decays exponentially with the Debye screening length κ^{-1}. Third, in near-critical polar binary fluids, the ion distributions and the critical fluctuations become highly heterogeneous around the colloid surfaces [22]. As a result, the wetting layer formation and the surface ionization are strongly coupled, which much complicates the colloid interaction.

On approaching the solvent criticality, the adsorption-induced interaction becomes long-ranged and universal [22–26], where the wall-induced heterogeneities extend over mesoscopic-length scales. In the film geometry, some universal scaling relations are well known and considerable efforts have been made to calculate [25,26] or measure [17,26,27] the so-called Casimir amplitudes (coefficients in universal relations) [28], In these papers, near-critical fluids at the critical composition have mostly been treated along the critical path. On the other hand, Maciołek *et al*. [29] found strong enhancement of one of the amplitudes in two-dimensional Ising films under an applied magnetic field. In accord with their finding, we have recently found growing of the amplitudes at off-critical compositions [30], which is particularly marked between a first-order capillary condensation line and the bulk coexistence line ($\mu_\infty = 0$) in the T-μ_∞ plane. We have then performed a simulation of phase separation around the capillary condensation line [31].

In this paper we aim to investigate the interaction between two neutral colloidal particles due to preferential adsorption in a near-critical binary mixture. We shall see that the solvent-mediated interaction is much enhanced when the component favored by the colloid surfaces is poor in the reservoir, as in

the case of the Casimir amplitudes. This is consistent with the observed aggregation of colloidal particles at off-critical compositions [7–10].

We also aim to examine the bridging transition between two colloidal particles [4,32], which is analogous to the capillary condensation transition in a film. That is, two large particles (or one large particle and a plate) are connected by the phase favored by the walls in bridged states, while they are disconnected by intrusion of the disfavored phase in separated states. Bridged states appear near the bulk coexistence curve as the separation distance is decreased. This phenomenon can well be expected to occur in colloid aggregation, so future experiments should be informative. As previous papers on bridging, we mention numerical calculations of phenomenological models [33,34], density functional theories [6,35], and a Monte Carlo study [36]. Also in water, a bubble bridging occurs between hydrophobic surfaces [37], which is related to predrying of hydrophobic surfaces [38]. Similarly, in the isotropic phase of liquid crystals, a nematic domain can appear between closely separated solid objects [39,40].

The organization of this paper is as follows. In Sec. II we will summarize the results of the local functional theory of near-critical binary mixtures. In Sec. III we will present a theory on the adsorption-induced interaction among colloidal particles together with some simulation results. In Sec. IV we will numerically investigate the bridging transition near the bulk criticality. In Appendix A we will examine how the grand potential is changed for small displacements of the colloid particles. In Appendix B we will apply the Derjaguin approximation to the adsorption-induced interaction.

II. RENORMALIZED GINZBURG-LANDAU FREE ENERGY

We consider near-critical binary mixtures using our local functional theory taking into account the renormalization effect near the bulk criticality, which is similar to the linear parametric model by Schofield *et al.* [41,42] and the local functional model by Fisher *et al.* [24,25]. These authors treated near-critical fluids outside the coexistence curve, while we define our model within its interior. Furthermore, our model satisfies the two-scale-factor universality [42]. The critical amplitude ratios from our model are in fair agreement with reliable estimates for Ising systems.

We assume an upper critical solution temperature T_c at a given average pressure. The order parameter ψ is proportional to $c - c_c$, where c is the composition and c_c is its critical value. The physical quantities exhibit singular dependence on ψ and the reduced temperature,

$$\tau = (T - T_c)/T_c. \tag{2.1}$$

Hereafter, $\alpha = 0.110$, $\beta = 0.325$, $\gamma = 1.240$, $\nu = 0.630$, $\eta = 0.0317$, and $\delta = 4.815$ are the usual critical exponents for Ising-like systems [42]. At the critical composition with $\tau > 0$, the correlation length is written as $\xi = \xi_0 \tau^{-\nu}$, where ξ_0 is a microscopic length. The coexistence curve in the region $\tau < 0$ is denoted by CX. We write ψ in the coexisting two phases as $\pm\psi_{\rm cx}$ with

$$\psi_{\rm cx} = b_{\rm cx}|\tau|^{\beta}, \tag{2.2}$$

where $b_{\rm cx}$ is a constant.

We set up the singular bulk free energy F_b, where the critical fluctuations with wave numbers larger than the inverse correlation length ξ^{-1} have been coarse-grained or renormalized. Including the square gradient term, F_b is of the local functional form [24,25,30],

$$F_b = \int d\boldsymbol{r}\left[f + \frac{1}{2}k_B T_c C|\nabla\psi|^2\right], \tag{2.3}$$

where the integral $\int d\boldsymbol{r}$ is within a cell. Outside CX ($|\psi| > \psi_{\rm cx}$ or $\tau \geqslant 0$), the singular free energy density $f = f(\psi,\tau)$ is written in the Ginzburg-Landau form,

$$f = k_B T_c\left(\tfrac{1}{2}r\psi^2 + \tfrac{1}{4}u\psi^4\right). \tag{2.4}$$

We do not write a constant term ($\propto|\tau|^{2-\alpha}$), which is a singular contribution for $\psi = 0$. In this paper, C is made dimensionless. Then, $\xi_0^{1/2}\psi$ is dimensionless, and $b_{\rm cx}$ in Eq. (2.2) is of order $\xi_0^{-1/2}$. In the mean field theory, C, r/τ, and u in F_b are constants independent of τ and ψ. In our renormalized functional theory, they depend on a nonnegative variable w representing the distance from the criticality in the τ-ψ plane. Outside CX, fractional powers of w appear as [43]

$$C = w^{-\eta\nu}, \tag{2.5}$$

$$r/\tau = \xi_0^{-2} w^{\gamma-1}, \tag{2.6}$$

$$u = u^* \xi_0^{-1} w^{(1-2\eta)\nu}, \tag{2.7}$$

where u^* is a universal number and is set equal to $2\pi^2/9$ in our numerical analysis.

From $\eta \ll 1$, we have $C \cong 1$. We determine w as a function of τ and ψ by

$$w = \tau + (3u^*\xi_0)w^{1-2\beta}\psi^2. \tag{2.8}$$

For $\psi = 0$, we simply have $w = \tau$. For $\tau = 0$, we obtain $w^{\beta} \propto |\psi|$, leading to the Fisher-Yang results [24]: $\xi \propto |\psi|^{-\nu/\beta}$ and $f \propto \xi^{-d} \propto |\psi|^{1+\delta}$. These authors introduced the local correlation length $\xi(\psi)$ for $\tau = 0$.

In our scheme ξ and the susceptibility χ are related to the second derivative $f'' = \partial^2 f/\partial\psi^2$ by

$$k_B T_c C/\xi^2 = k_B T_c/\chi = f''. \tag{2.9}$$

For $\tau > 0$ and $\psi = 0$, we find $\chi(\tau,0) = \xi_0^2\tau^{-\gamma}$. On approaching CX ($\psi \to \psi_{\rm cx}$), we require $f' = \partial f/\partial\psi \to 0$ to obtain $b_{\rm cx} = 1.50/(3u^*\xi_0)^{1/2}$ and $w = 1.714|\tau|$. The susceptibility on CX is determined by τ and is written as

$$\chi_{\rm cx} = \chi(\tau,\psi_{\rm cx}) = R_\chi \xi_0^2|\tau|^{-\gamma}, \tag{2.10}$$

with $R_\chi = 8.82$. The correlation length on CX is written as $\xi_{\rm cx} = 0.334\xi_0|\tau|^{-\nu}$.

We also need to determine f inside CX ($|\psi| < \psi_{\rm cx}$ and $\tau < 0$) to discuss phase separation. Its simplest form is

$$f = f_{\rm cx} + k_B T_c\left(\psi^2 - \psi_{\rm cx}^2\right)^2/\left(8\chi_{\rm cx}\psi_{\rm cx}^2\right), \tag{2.11}$$

where $f_{\rm cx}$ is the free energy density on CX. Then f, f', and f'' are continuous across CX. We also set $C = C_{\rm cx} = |\sigma_{\rm cx}\tau|^{-\eta\nu}$ inside CX, which is the value of C in Eq. (2.5) on CX. Here we neglect the thermal fluctuations longer than $\xi_{\rm cx}$. In our applications the space regions inside CX are not wider than $\xi_{\rm cx}$, and the ψ^4 form in Eq. (2.11) is well justified. As an

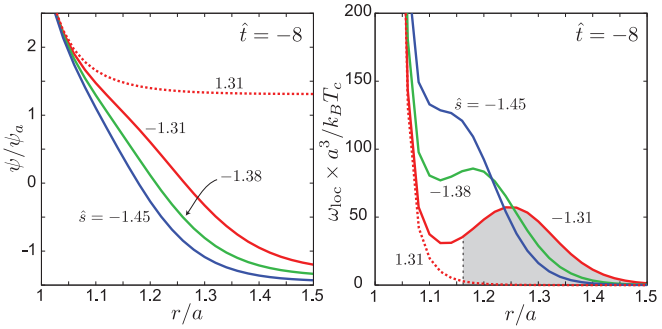

FIG. 1. (Color online) Normalized order parameter $\psi(r)/\psi_a$ (left) and normalized grand potential density $\omega_{\rm loc}(r)a^3/k_BT_c$ (right) vs r/a around a single colloid for $\hat{s} = \psi_\infty/\psi_a = 1.31, -1.31, -1.38$, and -1.45 with $\hat{t} = \tau(\xi_0/a)^{1/\nu} = -8$. Shaded area below the curve of $\hat{s} = -1.31$ is equal to the normalized surface tension $\sigma a^2/k_BT_c$. On CX, $\hat{s} = \pm 1.30$ and $\xi = 0.09a$ for $\hat{t} = -8$.

example, we may calculate the interface profile from Eqs. (2.3) and (2.11), where the surface tension is of the form [42],

$$\sigma = 0.075 k_B T_c/\xi_{\rm cx}^2. \tag{2.12}$$

We shall see another example inside CX in Fig. 1.

III. COLLOIDAL PARTICLES IN A NEAR-CRITICAL FLUID

We consider identical colloidal particles with common radius a much larger than ξ_0 in a near-critical binary mixture. We seek equilibrium profiles of $\psi(\boldsymbol{r})$ around these large particles. We assume $\psi \to \psi_\infty$ far from them, where ψ_∞ is proportional to the composition deviation $c_\infty - c_c$ far from the colloidal particles. In its calculation, we take the limit of strong preferential adsorption. This $\psi(\boldsymbol{r})$ minimizes the grand potential Ω, giving rise to attraction among the colloidal particles. Typical reduced temperatures in this paper are from -1 to -10 in units of $(\xi_0/a)^{1/\nu}$ and are very small for large a. Then the prewetting transition [20] may be assumed to occur at lower temperatures. In fact, we realize thick adsorption layers in our numerical analysis. Experimentally, strong preferential adsorption was observed on colloid surfaces in a near-critical fluid by light scattering [7].

A. Equilibrium relations

On the cell surface we assume $\boldsymbol{n}\cdot\nabla\psi = 0$ for simplicity, but on the colloid surfaces we assume

$$\boldsymbol{n}\cdot\nabla\psi = -h_1/C, \tag{3.1}$$

where $\boldsymbol{n}$ is the normal unit vector from the interior to the exterior and h_1 is a large positive surface field arising from the short-range, fluid-surface interaction. In equilibrium, we minimize the grand potential, consisting of the bulk term and the surface term as

$$\Omega = \int d\boldsymbol{r}\omega_{\rm loc} - k_BT_c\int dS h_1\psi. \tag{3.2}$$

Hereafter, $\int d\boldsymbol{r}$ is the space integral outside the colloidal particles and in the cell, while $\int dS$ is the surface integral on the colloid surfaces. We define the grand potential density including the gradient contribution,

$$\omega_{\rm loc} = f(\psi) - f_\infty - \mu_\infty(\psi - \psi_\infty) + k_BT_c\frac{C}{2}|\nabla a\psi|^2, \tag{3.3}$$

where $f_\infty = f(\psi_\infty)$ and μ_∞ is related to ψ_0 by

$$\mu_\infty = f'(\psi_\infty). \tag{3.4}$$

In particular, $\mu_\infty \cong (\psi_\infty + \psi_{\rm cx})/\chi_{\rm cx}$ close to the negative branch of CX. The $\omega_{\rm loc}$ is nonnegative in our case, tending to 0 far from the colloidal particles. Minimization of Ω yields Eq. (3.1) as the boundary condition and

$$\frac{\delta F_b}{\delta\psi} = f'(\psi) - k_BT_cC\nabla^2\psi - k_BT_c\frac{C'}{2}|\nabla\psi|^2 = \mu_\infty, \tag{3.5}$$

in the fluid region, where $C'(\psi) = dC/d\psi$.

In equilibrium, Ω is a function of the colloid centers $\boldsymbol{R}_\alpha = (R_{\alpha x}, R_{\alpha y}, R_{\alpha z})$ $(\alpha = 1,2,\dots)$. In Appendix A, we will derive the following equilibrium relation:

$$\frac{\partial\Omega}{\partial R_{\alpha i}} = \int_\alpha dS\sum_j(\Pi_{\psi ij} - \Pi_\infty\delta_{ij})n_{\alpha j}, \tag{3.6}$$

where $i,j = x,y,z$. The integral $\int_\alpha dS$ is on the surface of the αth colloidal particle and $\boldsymbol{n}_\alpha = (n_{\alpha x}, n_{\alpha y}, n_{\alpha z})$ is the normal unit vector from the colloid interior to the exterior. The $\Pi_{\psi ij}$ is the stress tensor due to the order parameter deviations given by [42]

$$\Pi_{\psi ij} = (\psi\delta F_b/\delta\psi - f - k_BT_cC|\nabla\psi|^2/2)\delta_{ij} + k_BT_cC(\nabla_i\psi)(\nabla_j\psi). \tag{3.7}$$

This tensor satisfies the relation

$$\sum_j\nabla_j\Pi_{\psi ij} = \psi\nabla_i(\delta F_b/\delta\psi), \tag{3.8}$$

which vanishes in equilibrium or under Eq. (3.5). Here $\Pi_{\psi ij} \to \Pi_\infty\delta_{ij}$ far from the colloidal particles with

$$\Pi_\infty = \psi_\infty\mu_\infty - f(\psi_\infty). \tag{3.9}$$

If we further use Eq. (3.5), we obtain a simpler expression:

$$\Pi_{\psi ij} = (\Pi_\infty - \omega_{\rm loc})\delta_{ij} + k_BT_cC(\nabla_i\psi)(\nabla_j\psi). \tag{3.10}$$

The expression (3.7) and the relation (3.8) are valid even in nonequilibrium and have in fact been used in dynamics [31,42]. Note that the total stress tensor may be expressed as $p_0\delta_{ij} + \Pi_{\psi ij}$ in binary mixtures, where p_0 is a large background pressure nearly uniform in the cell (with small variations arising from sounds and gravity).

B. Scaling for strong adsorption

We make Eq. (3.5) dimensionless by scaling the position $\boldsymbol{r}$ by a and ψ by ψ_a, where ψ_a is is a characteristic order parameter around the colloidal particles of the form

$$\psi_a = (\sqrt{24}\xi_0/a)^{\beta/\nu}/(3u^*\xi_0)^{1/2}. \tag{3.11}$$

Use of b_{cx} in Eq. (2.2) gives $\psi_a = 1.47 b_{cx}(\xi_0/a)^{\beta/\nu}$. By scaling τ and ψ_∞, we introduce two parameters:

$$\hat{t} = \tau(a/\xi_0)^{1/\nu}, \tag{3.12}$$

$$\hat{s} = \psi_\infty/\psi_a. \tag{3.13}$$

The scaled correlation length ξ/a is given by $\hat{t}^{-\nu}$ for $\tau > 0$ on the critical path, $0.13|\hat{s}|^{-\nu/\beta}$ for $\tau = 0$, and $0.3|\hat{t}|^{-\nu}$ on CX. The CX curve is expressed as $\hat{s} = \pm\hat{s}_{cx}$ with $\hat{s}_{cx} = \psi_{cx}/\psi_a = 0.66|\hat{t}|^\beta$ from Eq. (2.2). In our calculations we may use the scaled quantities only, where we need not specify the ratio $\xi_0/a \ll 1$. The scaling factors $\tau/\hat{t} = (\xi_0/a)^{1/\nu}$ and $\psi_\infty/b_{cx}\hat{s} = 1.47(\xi_0/a)^{\beta/\nu}$ are needed when our theoretical results are compared with experimental data. For example, if $a/\xi_0 = 10^4$, they are 0.40×10^{-6} and 0.011, respectively.

We write the value of ψ on the colloid surfaces as ψ_0. For sufficiently large ψ_0, the near-wall behaviors of ψ and ω_{loc} are expressed as [24,30,44]

$$\psi \sim \xi_0^{\beta/\nu-1/2}(\lambda + \ell_0)^{-\beta/\nu}, \tag{3.14}$$

$$\omega_{loc} \sim k_B T_c(\lambda + \ell_0)^{-3}, \tag{3.15}$$

where λ is the distance from such a surface. We here assume that λ is shorter than the correlation length $\xi = \xi(\tau, \psi_\infty)$ far from the surface. The length ℓ_0 is of the order of the local correlation length near the surface ($\propto \psi_0^{-\nu/\beta}$) [24]. In terms of b_{cx} in Eq. (2.2), we have

$$\ell_0 = 0.544\xi_0(b_{cx}/\psi_0)^{\nu/\beta}, \tag{3.16}$$

where we assume $b_{cx}^{-1}\psi_0 \sim \xi_0^{1/2}\psi_0 \ll 1$ so $\ell_0 \gg \xi_0$. In terms of ψ_a, we also have $\ell_0/a = (\beta/2\nu)(\psi_a/\psi_0)^{\nu/\beta}$. For $\lambda \gg \ell_0$, ψ and ω_{loc} become independent of ℓ_0 or ψ_0. From Eq. (3.1), we obtain the scaling relation,

$$h_1 \sim C(\psi_0)\psi_0/\ell_0 \sim \psi_0^{\delta-\nu/\beta}, \tag{3.17}$$

where $\delta - \nu/\beta = (3-\eta)/(1+\eta) \cong 3$. The strong adsorption condition $\xi_0^{1/2}\psi_0 \gg |\tau|^\beta$ is realized with increasing h_1 or on approaching the bulk criticality. In our numerical analysis, we assume $h_1/C(\psi_0) = 170\psi_a/a$ to obtain $\psi_0/\psi_a \sim 10$. See Fig. 1 for the near-wall behaviors of ψ and ω_{loc} in the strong adsorption.

The integral of ψ in the near-wall layers with $0 < \lambda < \ell_0$ is proportional to $\psi_0\ell_0 \sim \psi_0^{1-\nu/\beta}$ and becomes negligible for large ψ_0 (since $\nu/\beta \sim 2$), while that in the region $\ell_0 < \lambda < \xi(\tau, \psi_\infty)$ grows as $\xi^{1-\beta/\nu}$(critical adsorption) [20]. It follows a well-defined preferential adsorption,

$$\Gamma = \int d\boldsymbol{r}[\psi(\boldsymbol{r}) - \psi_\infty], \tag{3.18}$$

which is independent of h_1 for large h_1. On the other hand, the integral of ω_{loc} in the layers with $0 < \lambda < \ell_0$ and the surface free energy in Eq. (3.2) ($\propto h_1$) are both proportional to $\psi_0^{2\nu/\beta}$ and are large in magnitude. However, they are constants nearly independent of τ and ψ_∞ and are irrelevant in the capillary condensation and the bridging transition [see discussion below Eq. (3.25)], which much simplifies our results.

C. Adsorption on a single colloidal particle

In the strong adsorption regime, the profile of ψ is highly nontrivial for negative ψ_∞, since ψ changes from a large positive value near the surface to $\psi_\infty < 0$ far from it. To illustrate this aspect, we here consider the simplest case of a single spherical particle [45], where $\psi(r)$ is a function of the distance r from the particle center. In this case, if ψ_∞ approaches the CX value $-\psi_{cx}$ under the condition $\xi \cong \xi_{cx} \ll a$, the thickness of the adsorption layer increases logarithmically with increasing a as [45]

$$\xi_{ad} \sim \xi \ln(a/\xi). \tag{3.19}$$

Here the contribution to Ω from the transition region ($r - a \sim \xi_{ad}$) is of order $4\pi a^2\sigma$, where $\sigma(\propto|\tau|^{2\nu})$ is the surface tension.

In Fig. 1, $\psi(r)/\psi_a$ and $\omega_{loc}(r)a^3/k_BT_c$ are displayed around a single colloidal particle for $\hat{t} = -8$, where use is made of the free energy density f inside CX in Eq. (2.11) for $\hat{s} < 0$. Note that $\hat{s} = \pm\hat{s}_{cx} = \pm 1.30$ on the positive and negative branches of CX. (1) For $\hat{s} = 1.31$, the thickness of the adsorption layer is given by $\xi = 0.09a$. For $\hat{s} = -1.31$, it is thicker than ξ by a few times and is of order ξ_{ad} in Eq. (3.19). This distinct difference of adsorption between these two compositions was detected by Beysens *et al.* [7] by light scattering. (2) Furthermore, for $\hat{s} = -1.31$, the curve of $\omega_{loc}(r)a^3/k_BT_c$ in Fig. 1 exhibits a peak at $r/a - 1 \sim \xi_{ad}/a$ with its area being about $\sigma a^2/k_BT_c$. However, the peak recedes and diminishes for smaller $\hat{s}$ (-1.38 and -1.45 in Fig. 1).

In passing, we mention the observed partitioning of the colloidal particles between coexisting two phases [7,8]. For dilute colloidal particles, their density in the favored phase is higher than that in the disfavored phase by $\exp(\Delta F_{sol}/k_BT)$, where ΔF_{sol} is the difference of the grand potentials Ω at $\hat{s} = \pm s_{cx}$ around a single colloidal particle. From Fig. 1 it is estimated as

$$\Delta F_{sol} \cong 4\pi\sigma(a + \xi_{ad})^2 \sim k_BT_c|\hat{t}|^{2\nu}, \tag{3.20}$$

which means that the colloidal particles mostly move into the favored phase for $|\hat{t}| \gg 1$. For example, for $\hat{t} = -8$, we obtain $\Delta F_{sol}/k_BT_c = 1.9 \times 4\pi\sigma a^2/k_BT_c = 228$, where the factor 1.9 is due to $\xi_{ad}/a \sim 0.3$ (see Fig. 1). Note that ΔF_{sol} is independent of h_1 in the present strong adsorption, while $\Delta F_{sol} \propto h_1$ in the weak adsorption [46]. The ΔF_{sol} here is an example of the Gibbs transfer free energy (usually defined for ions) [16,22,47], which is the difference of the solvation chemical potentials of solute in two coexisting phases of solvent.

D. Two colloidal particles

As in Fig. 2, we consider two colloidal particles with equal radius a. In our numerical analysis, they are placed in the middle of a cylindrical cell with radius $R_0 = 8a$ and height $H_0 = 16a$. The system is then in the region $0 < (x^2 + y^2)^{1/2} < R_0$ and $0 < z < H_0$. The particle centers are at $(0,0, \pm(\ell/2 + a))$ with ℓ being the surface-to-surface separation distance. Hereafter, we set

$$\hat{\ell} = \ell/a. \tag{3.21}$$

When the system lengths (R_0 and L_0) much exceed a, it is convenient to write Ω as

$$\Omega = \Omega_\infty - k_BT_c\mathcal{G}, \tag{3.22}$$

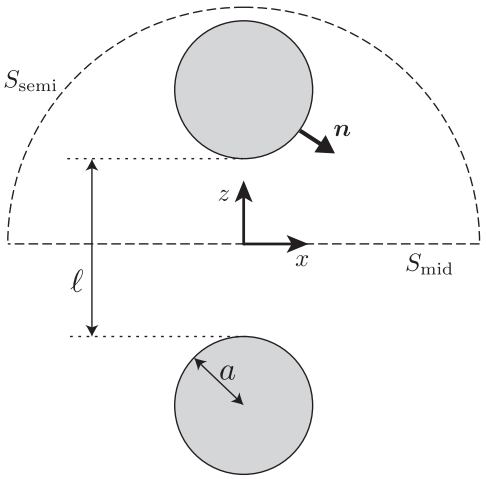

FIG. 2. Geometry of two identical spherical colloidal particles with radius a and separation ℓ in the xz plane. Surfaces $S_{\rm mid}$ and $S_{\rm semi}$ are introduced in Appendix A.

where Ω_∞ is the value of Ω for $\ell \gg a$. That is, $\Omega_\infty = 2\Omega_1$, where Ω_1 is the grand potential for one isolated colloidal particle. The dimensionless quantity $\mathcal{G}$ is a universal function of $\hat{t}$, $\hat{s}$, and $\hat{\ell}$ decaying to 0 for large $\hat{\ell}$. Note that it is independent of h_1 in the strong adsorption limit, as discussed in Sec. III B. The adsorption-induced force between the two colloidal particles is given by

$$\frac{\partial \Omega}{\partial \ell} = \frac{k_B T_c}{a}\mathcal{F}. \tag{3.23}$$

The dimensionless functions $\mathcal{F}(\hat{\ell})$ and $\mathcal{G}(\hat{\ell})$ are related by

$$\mathcal{F} = -\frac{\partial}{\partial \hat{\ell}}\mathcal{G}. \tag{3.24}$$

We also have $\mathcal{G}(\hat{\ell}) = \int_{\hat{\ell}}^{\infty} d\hat{\ell}'\mathcal{F}(\hat{\ell}')$. In the derivative and the integral with respect to $\hat{\ell}$, $\hat{t}$ and $\hat{s}$ are fixed.

As will be shown in Appendix A, Eqs. (3.6) and (3.10) yield a convenient form for the normalized force $\mathcal{F}$,

$$\mathcal{F} = \frac{a}{k_B T_c}\int dx\, dy \omega_{\rm loc}(x,y,0), \tag{3.25}$$

where the integral is on the xy plane with $z = 0$ (the midplane between the two colloidal particles). Here the integral $\int dxdy$ may be replaced by $2\pi \int drr$, since $\omega_{\rm loc}(x,y,0)$ depends only on $r = (x^2 + y^2)^{1/2}$. If $\ell \gg \ell_0$, the midplane is far from the transition layers with thickness ℓ_0 and $\omega_{\rm loc}(x,y,0)$ becomes independent of ψ_0 or h_1. In this paper we thus calculate $\mathcal{F}$ from Eq. (3.25).

We may use Eq. (3.15) on the midplane between the two colloidal particles for small ℓ [48], where we set $\lambda = \ell + r^2/a \gg \ell_0$. From Eq. (3.25) we thus find

$$\mathcal{F} \sim a\int_0^\infty drr(\ell + r^2/a)^{-3} \sim \hat{\ell}^{-2}, \tag{3.26}$$

where the integral in the range $r \lesssim (\ell a)^{1/2} (\ll a)$ is dominant. To be precise, Eq. (3.25) gives $\lim_{\hat{\ell}\to 0}\hat{\ell}^2\mathcal{F} = 0.205\pi$ as the coefficient in Eq. (3.26). In Appendix B the Derjaguin approximation [3,4,19] for small $\hat{\ell}$ will yield

$$\mathcal{G} \cong \pi\Delta_{\rm cri}\hat{\ell}^{-1}, \quad \mathcal{F} \cong \pi\Delta_{\rm cri}\hat{\ell}^{-2}, \tag{3.27}$$

with $\Delta_{\rm cri} \cong 0.279$. The coefficient $\pi\Delta_{\rm cri}$ is somewhat larger than that from Eq. (3.25). This small-$\hat{\ell}$ behavior stems from the de Gennes-Fisher theory for near-critical films [17,23,26]. Furthermore, in Appendix B, we shall see that if ℓ exceeds the correlation length ξ without bridging, $\mathcal{F}$ and $\mathcal{G}$ decay exponentially as

$$\mathcal{F} \sim (a/\xi)^2 e^{-\ell/\xi}, \quad \mathcal{G} \sim (a/\xi)e^{-\ell/\xi}, \tag{3.28}$$

where ξ is determined by τ and ψ_∞ from Eq. (2.9). These relations follow in separated states where ψ at the midpoint ($\boldsymbol{r} = \boldsymbol{0}$) is close to ψ_∞ [30].

Note that Eq. (3.27) holds for $\hat{\ell} \lesssim \xi/a$ and Eq. (3.28) for $\xi/a \lesssim \hat{\ell} \ll 1$. However, the exponential decays in Eq. (3.28) are observed even for $\hat{\ell} \sim 1$ in our numerical analysis (see Figs. 5 and 6). The same exponential form of $\mathcal{G}$ was found in the previous papers [10,26,49].

E. Numerical results without bridging transition

In Figs. 3–6, we present numerical results where there is no bridging transition. We aim to show that $\mathcal{G}$ and $\mathcal{F}$ are much more enhanced for $\hat{s} < 0$ than for $\hat{s} > 0$.

In the left panel of Fig. 3, we show curves of $\hat{\ell}^2\mathcal{F}$ vs $\hat{\ell}$ calculated from Eq. (3.25) and those from the Derjaguin approximation for $(\hat{\tau},\hat{s}) = (0,-1)$ and $(5,0)$. They tend to a constant as $\hat{\ell} \to 0$ as in Eqs. (3.26) and (3.27). Remarkably, for $\hat{s} < 0$ and $\hat{t} = 0$, $\hat{\ell}^2\mathcal{F}$ increases up to of order 10 to exhibit a peak as a function of $\hat{\ell}$, where the peak position is at $\ell \cong 6.14\xi$ from Eq. (B15). On the other hand, for $\hat{t} > 0$ and $\hat{s} = 0$, $\hat{\ell}^2\mathcal{F}$ exhibits only a rounded maximum of order 1 at $\ell \sim 1.64\xi$ from Eq. (B17). We recognize that the force is much enhanced for negative $\hat{s}$, and the Derjaguin approximation nicely holds for $\hat{\ell} \lesssim 1$. In the right panel of Fig. 3, we present $\psi(x,0,z)/\psi_a$ in gradation for $(\hat{\tau},\hat{s},\hat{\ell}) = (0,-1,0.4)$ in the xz plane, where ψ is large in the region between the two colloidal particles.

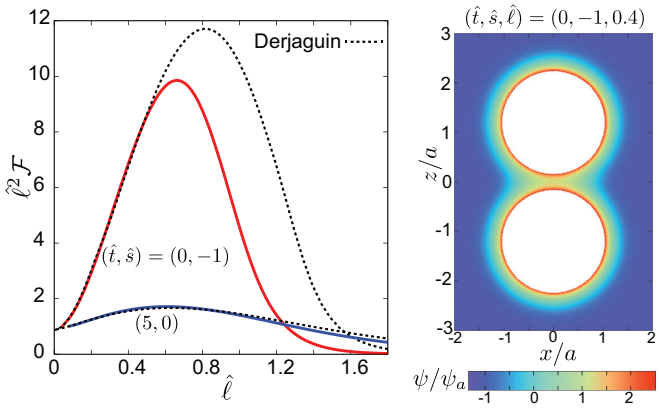

FIG. 3. (Color online) Left: $\hat{\ell}^2\mathcal{F}$ vs $\hat{\ell} = \ell/a$ for $(\hat{t},\hat{s}) = (0,-1)$ (red bold line) and $(5,0)$ (blue bold line), where the correlation length ξ is $0.13a$ for the former and $0.36a$ for the latter. The normalized force $\mathcal{F}$ is calculated from Eq. (3.25). Curves from the Derjaguin approximation in Eq. (B8) are also written (dotted lines). Right: Normalized order parameter $\psi(x,0,z)/\psi_a$ on the xz plane according to the color bar below for $(\hat{t},\hat{s},\hat{\ell}) = (0,-1,0.4)$. For these $(\hat{t},\hat{s})$, no bridging transition occurs for any $\hat{\ell}$.

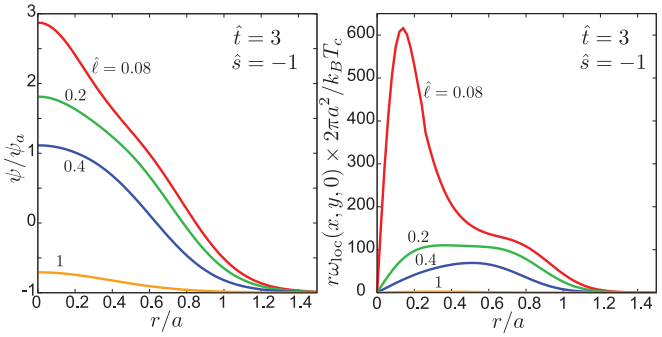

FIG. 4. (Color online) Midplane behaviors of $\psi(r,0)/\psi_a$ (left) and $r\omega_{\rm loc}(r,0)\times 2\pi a^2/k_BT_c$ (right) as functions of $r/a=(x^2+y^2)^{1/2}/a$ at $z=0$ for $(\hat{t},\hat{s})=(3,-1)$ with $\xi/a=0.12$. Here $\hat{\ell}$ decreases as 1.0,0.4, 0.2, and 0.08. Then, $\psi(0,0)/\psi_a$ at the midpoint is equal to -0.707, 1.11, 1.81, and 2.87, respectively, while $\mathcal{F}$ grows dramatically as 1.11, 44.1, 86.5, and 219, respectively. Area below each curve (left) is equal to $\mathcal{F}$.

In Fig. 4, for $(\hat{\tau},\hat{s})=(3,-1)$, we show $\psi(r,0)/\psi_a$ and $r\omega_{\rm loc}(r,0)\times 2\pi a^2/k_BT_c$ vs $r/a=(x^2+y^2)^{1/2}/a$ at $z=0$. We change $\hat{\ell}$ as 1, 0.4, 0.2, and 0.008. For $\hat{\ell}=1$, the two colloidal particles are so separated such that $\psi(r,0)<0$ resulting in a small $\mathcal{F}=1.1$. On the other curves of smaller $\hat{\ell}$, $\psi(r,0)$ decreases from positive to negative with increasing r and $\mathcal{F}$ increases dramatically up to 219. The behavior of the latter curves is consistent with the theoretical expressions $\psi\propto[\hat{\ell}+(r/a)^2]^{-\beta/\nu}$ and $\omega_{\rm loc}\propto[\hat{\ell}+(r/a)^2]^{-3}$, at $z=0$, which follow from Eqs. (3.14) and (3.15) with $\lambda=\ell+r^2/a\gg\ell_0$ as in Eq. (3.26).

Next, we plot $\mathcal{G}$ and $\mathcal{F}$ vs $\hat{\ell}$ for six values of $\hat{s}$ at $\hat{\tau}=0$ in Fig. 5 and for five values of $(\hat{t},\hat{s})$ with $\hat{\tau}>0$ in Fig. 6 on semilogarithmic scales. In these examples, there is no bridging transition for any $\hat{\ell}$. For small $\hat{\ell}$, we have the behaviors in Eq. (3.27). For relatively large $\hat{\ell}$ ($\xi\ll\ell\lesssim a$), both $\mathcal{G}$ and $\mathcal{F}$ decay exponentially as $\exp(-\ell/\xi)$. We confirm that the slopes of these curves are close to a/ξ for $\hat{\ell}\sim 1$, where ξ is calculated from Eq. (2.9). We can again see that $\mathcal{F}$ is well approximated by the Derjaguin approximation for $\hat{\ell}\lesssim 1$.

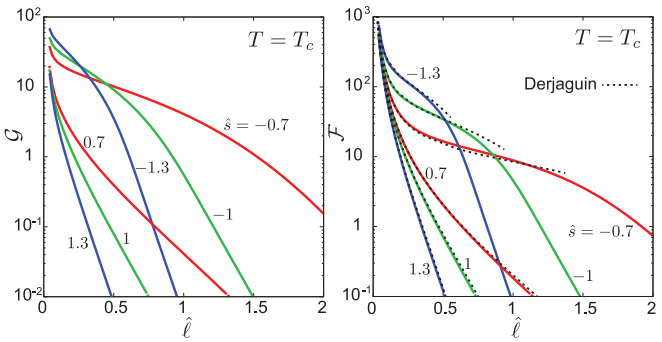

FIG. 5. (Color online) Normalized interaction free energy $\mathcal{G}$ (left) and normalized force $\mathcal{F}$ (left) vs $\hat{\ell}$ at $\hat{t}=0$ for $\hat{s}=-1.3$, -1, -0.7, 0.7, 1, and 1.3. Curves from the Derjaguin approximation (dotted lines) are also written for $\mathcal{F}$ (right). These quantities are much larger for $\hat{s}<0$ than for $\hat{s}>0$ for not very small $\hat{\ell}$. The slopes of the curves are close to $-a/\xi$ for relatively large $\hat{\ell}$ from Eq. (3.28). Here there is no bridging transition.

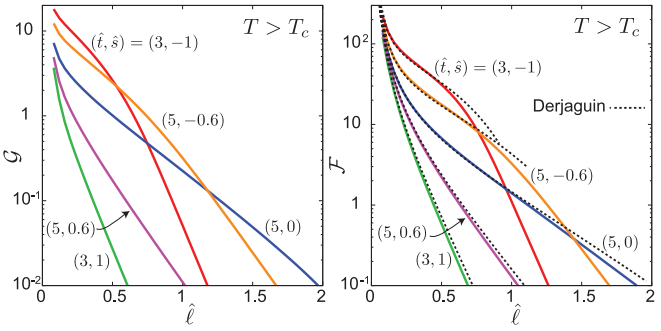

FIG. 6. (Color online) $\mathcal{G}$ (left) and $\mathcal{F}$ (left) vs $\hat{\ell}$ for $(\hat{t},\hat{s})=(3,-1)$, $(5,-0.6)$, (5,0), (5,0.6), and (3,1) with $\hat{t}>0$. Curves from the Derjaguin approximation (dotted lines) are also written for $\mathcal{F}$ (right). As in Fig. 5, they strongly depend on the sign of $\hat{s}$, with the slopes being $-a/\xi$ for relatively large $\hat{\ell}$. Here there is no bridging transition.

F. Van der Waals interaction

So far, we have not explicitly accounted for the pairwise van der Waals interaction [3] among constituent molecules, which was treated as one of the main elements causing colloid aggregation [7,50]. The resultant potential $U_{\rm vdw}(r)$ between two colloidal particles with equal radius a is written as [4,19]

$$U_{\rm vdw}=-\frac{A_{\rm H}}{6}\left[\frac{2a^2}{r^2-4a^2}+\frac{2a^2}{r^2}+\ln\left(1-\frac{4a^2}{r^2}\right)\right], \tag{3.29}$$

where $r=2a+\ell$ is the center-to-center distance. The Hamaker constant $A_{\rm H}$ is in many cases of order 10^{-19} J, but it can change its sign [3,20] and can be very small for some systems of colloids and binary mixtures [10]. Without charges, the total potential is of the form

$$U_{\rm tot}=-k_BT_c\mathcal{G}+U_{\rm vdw}, \tag{3.30}$$

consisting of the adsorption-induced part and the van der Waals part. The former is very sensitive to τ and ψ_∞ in the critical ranges, while the latter is insensitive to them. If we further include the charge effects, we should add an appropriate charge-induced interaction U_C in Eq. (3.30) [7,10,17,22,26] [see item (3) in Sec. V for more discussions].

The force from the van der Waals interaction reads

$$F_{\rm vdw}=\frac{d}{dr}U_{\rm vdw}=\frac{32A_Ha^6}{3\ell^2r^3(r+2a)^2}. \tag{3.31}$$

As $\hat{\ell}\to 0$, we find $F_{\rm vdw}\cong A_{\rm H}/12a\hat{\ell}^2$. This behavior is the same as that of $\mathcal{F}$ in Eq. (3.27). So we compare the coefficients in front of the power $\hat{\ell}^{-2}$ of the two forces, $A_{\rm H}/12a$ and $\pi\Delta_{\rm cri}\times k_BT_c/a$, to obtain the ratio

$$R_{\rm vdw}=A_H/(12\pi k_BT_c\Delta_c), \tag{3.32}$$

where the denominator is 0.4×10^{-19}J for $T_c\cong 300$ K. If $|A_{\rm H}|$ is smaller than 0.4×10^{-19} J, we have $|R_{\rm vdw}|<1$ and the van der Waals interaction is weaker than the adsorption-induced interaction at least for small $\hat{\ell}$.

However, $\hat{\ell}^2\mathcal{F}$ grows for $\hat{s}<0$ with increasing $\hat{\ell}$ as in Fig. 3, so we need to examine the relative importance of the van der Waals interaction and the adsorption-induced interaction for larger $\hat{\ell}$. To this end, in Fig. 7, we plot $\hat{\ell}^2\mathcal{F}/\pi\Delta_{\rm cri}$ for four

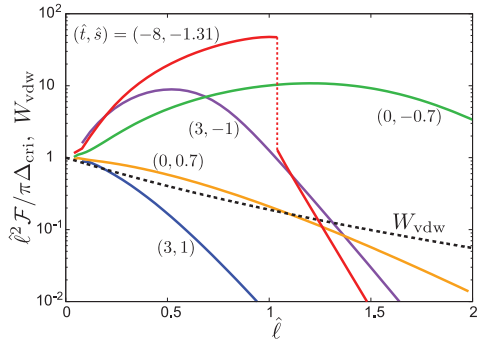

FIG. 7. (Color online) $\hat{\ell}^2\mathcal{F}/\pi\Delta_{\rm cri}$ (bold line) and $W_{\rm vdw}$ (dotted line) in Eq. (3.33) as functions of $\hat{\ell}$ on a semilogarithmic scale for $(\hat{t},\hat{s}) = (3,-1)$, $(0,-0.7)$, $(0,0.7)$, $(3,1)$, and $(-8,-1.31)$. These curves start from 1 at $\hat{\ell} = 0$. For $\hat{\ell} \sim 1$, $\hat{\ell}^2\mathcal{F}/\pi\Delta_{\rm cri}$ is of order 10 for negative $\hat{s}$ without bridging and is even of order 100 at the bridging transition, much exceeding $W_{\rm vdw}$. A bridging transition occurs for $(\hat{t},\hat{s}) = (-8,-1.31)$ at $\hat{\ell} = 1.04$.

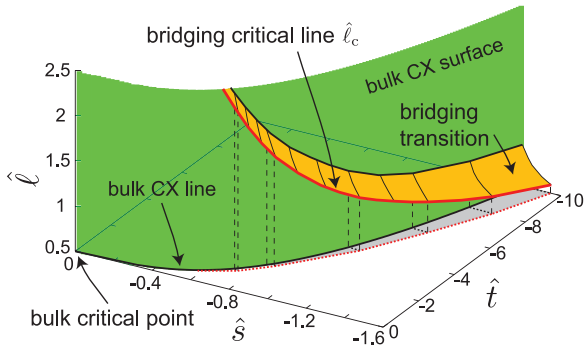

FIG. 8. (Color online) Phase diagram in the $\hat{t}$-$\hat{s}$-$\hat{\ell}$ space outside the bulk coexistence surface (CX) (green), where a surface of a first-order bridging transition (orange) is bounded by CX and a bridging critical line (red). The critical line approaches CX tangentially at $(\hat{t},\hat{s},\hat{\ell}) = (-1,-0.66,2.6)$.

typical cases together with

$$W_{\rm vdw} \equiv \frac{12}{A_H a}\ell^2 F_{\rm vdw} = \frac{128}{(\hat{\ell}+2)^3(\hat{\ell}+4)^2}. \tag{3.33}$$

In Fig. 7, while all the curves start from unity for $\hat{\ell} \to 0$, the normalized quantity $\hat{\ell}^2\mathcal{F}/\pi\Delta_{\rm cri}$ increases up to a maximum about 10 for $\hat{s} < 0$ without bridging formation and can even be of order 100 close to a bridging transition with increasing $\hat{\ell}$. Thus, at off-critical compositions with $\hat{s} < 0$, the adsorption-induced interaction can well dominate over the van der Waals interaction (even for $|A_{\rm H}| \sim 10^{-19}$ J).

IV. BRIDGING TRANSITION BETWEEN TWO COLLOIDAL PARTICLES

In this section we study the bridging transition for $\hat{s} < 0$ between two colloidal particles in a near-critical binary mixture. In our case ψ assumes the profiles of $\hat{s} < 0$ in Fig. 1 in separated states, where the adsorption layer has a thickness of order $\xi_{\rm av}$ in Eq. (3.19). A bridging transition can then occur in a wide range of $\ell(<2.6a)$ for $\hat{t} < -1.0$ with $\xi/a \sim 0.3|\hat{t}|^{-\nu} < 1$. In the previous papers [6,33–36], bridging between two spheres or between a sphere and a plate were studied numerically for small separation ℓ (say, $\sim 0.2a$) far from the criticality.

A. Phase diagrams

In Fig. 8 we first show a phase diagram of the bridging transition in the $\hat{t}$-$\hat{s}$-$\hat{\ell}$ space outside CX. We find a surface of a first-order bridging transition, bounded by CX and a bridging critical line. As functions of $(\hat{t},\hat{s})$, the normalized separation $\hat{\ell}$ may be written on the transition surface and on the critical line as

$$\hat{\ell} = \hat{\ell}_{\rm tr}(\hat{t},\hat{s}), \quad \hat{\ell} = \hat{\ell}_c(\hat{t}), \tag{4.1}$$

respectively. We also have $\hat{s} = \hat{s}_c(\hat{t})$ on the critical line. In the original units we have $\ell_{\rm tr} = a\hat{\ell}_{\rm tr}$ on the transition surface and $\ell_c = a\hat{\ell}_c$ on the critical line. Across this surface, discontinuities appear in $\mathcal{F}$ and the adsorption Γ in Eq. (3.18), which tend to vanish on approaching the critical line. The critical line tangentially ends on CX at $(\hat{t},\hat{s},\hat{\ell}) \cong (-1.0,-0.66,2.6)$. The maximum of $\hat{\ell}$ at a transition is thus 2.6.

In Fig. 9 phase diagrams in the $\hat{t}$-$\hat{s}$ and $\hat{t}$-μ_∞/μ_a planes are presented, where μ_∞ is related to ψ_∞ by Eq. (3.4) and scaled by $\mu_a = k_B T_c/a^3\psi_a$. In these phase diagrams, a first-order bridging transition occurs at some $\hat{\ell}$ in the region between CX and the bridging critical line, where the latter approaches CX tangentially. We also write cross-sectional bridging transition lines at fixed ℓ (equal to 1.4 and 1.04) on the bridging transition surface, each starting from CX and ending at a point on the critical line. In our case, these lines are nearly straight in the two phase diagrams in Fig. 9. Previously, bridging transition lines at fixed separation ℓ were drawn [26,33,35]. For near-critical films, on the other hand, the capillary condensation line is detached from CX. As a result, it is considerably curved in the τ-ψ_∞ plane [30], but is nearly straight in the τ-μ_∞ plane [31].

The phase behavior at fixed separation ℓ is particularly intriguing. In the left panel of Fig. 10, we show a phase diagram in the $\hat{t}$-$\hat{\ell}$ plane, where we write the critical line $\hat{\ell} = \hat{\ell}_c(\hat{t})$ and the transition line $\hat{\ell} = \hat{\ell}_{\rm cx}(\hat{t})$ on CX. The latter is defined by

$$\hat{\ell}_{\rm cx}(\hat{t}) = \hat{\ell}_{\rm tr}(\hat{t},-\hat{s}_{\rm cx}(\hat{t})), \tag{4.2}$$

where $-\hat{s}_{\rm cx}(\hat{t}) = -0.68|\hat{t}|^{\beta/\nu}$ is the vallue of $\hat{s}$ on the negative branch of CX. These two lines merge at $(\hat{t},\hat{\ell}) = (-1.0,2.6)$ on CX. Then let us vary $\hat{s}$ at fixed $\hat{\ell}$ and $\hat{t}$. (1) If $\hat{\ell} > \hat{\ell}_{\rm cx}(\hat{t})$, separated states are realized without bridging for any $\hat{s}$. (2) If $\hat{\ell}_{\rm cx}(\hat{t}) > \hat{\ell} > \hat{\ell}_{\rm cx}(\hat{t})$, we encounter the transition surface at a certain $\hat{s}$ to find a discontinuous change. (3) For $\hat{\ell} < \hat{\ell}_{\rm cx}(\hat{t})$, a bridging domain appears with a well-defined interface close to CX, but disconnection occurs continuously with increasing the distance from CX. In this changeover, it is puzzling how the interface becomes ill-defined gradually (see Fig. 17).

In the right panel of Fig. 10, we plot the bridging radius r_b vs $\hat{\ell}$ at $\hat{t} = -8$ for $\hat{s} = -1.31, -1.35$, and -1.4, which correspond to the three marked points in the top panel of Fig. 9. We determine r_b from the condition $\psi(r_b,0) = 0$ at $z = 0$, where $\psi(r,0)$ changes from positive to negative at $r = r_b$ with a bridging domain in the range $\hat{\ell} < \hat{\ell}_{\rm tr}(\hat{t},\hat{s})$. As a function of ℓ at each $(\hat{t},\hat{s})$, r_b is shortest at the transition and increases with decreasing $\hat{\ell}$. It is about a for sufficiently small $\hat{\ell}$. Also it is

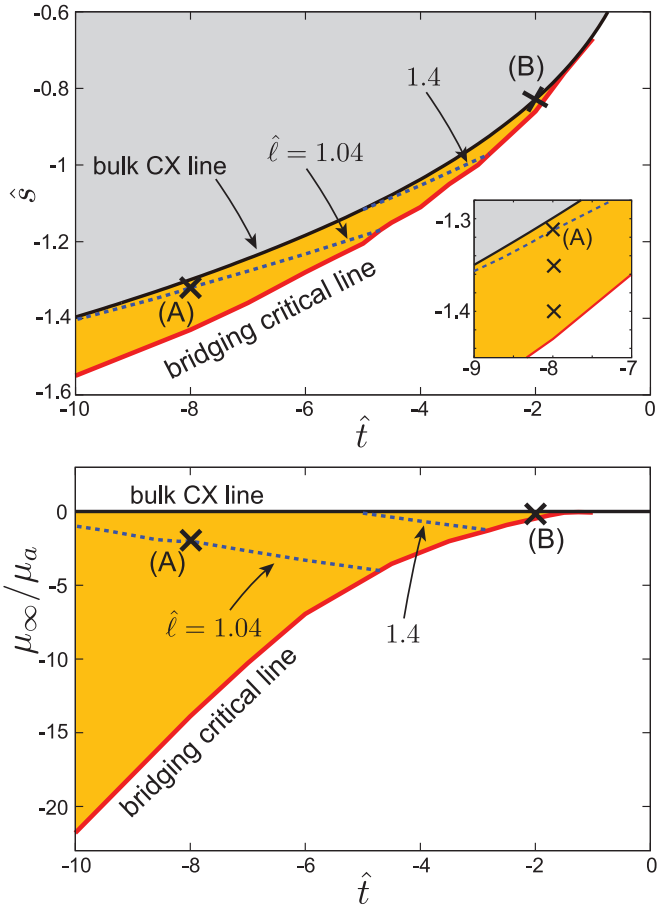

FIG. 9. (Color online) Phase diagrams in the $\hat{t}$-$\hat{s}$ plane (top) and in the $\hat{t}$-μ_∞/μ_a plane (middle), where $\mu_a = k_B T_c/a^3\psi_a$. A bridging transition occurs at some $\hat{\ell}$ in the region between CX and the bridging critical line. Shown also are cross-sectional bridging transition lines at fixed $\hat{\ell} = 1.4$ and 1.04 (blue dotted lines). In the inset (top), a region around $\hat{t} = -8$ is expanded. Particularly for bridging behaviors at point (A), point (B), and three points × (inset), see the following figures.

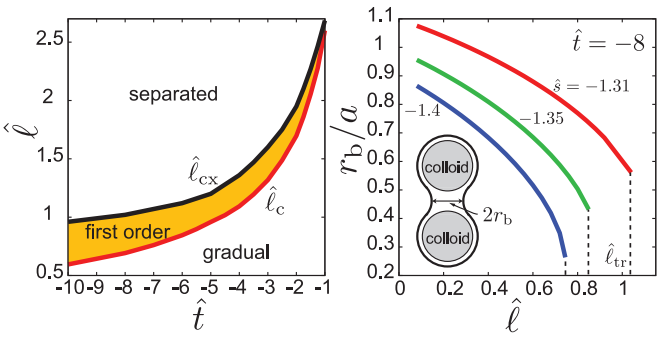

FIG. 10. (Color online) Left: Phase diagram in the $\hat{t}$-$\hat{\ell}$ plane, where the transition line on CX and and the critical line are written. Separated states are realized for any $\hat{s}$ above the transition line, a first-order bridging transition occurs for some $\hat{s}$ between the two lines, and the changeover is continuous or gradual for any $\hat{s}$ below the critical line. Right: Bridging radius r_b vs $\hat{t}$ at $\hat{t} = -8$ for $\hat{s} = -1.31, -1.35$, and -1.4 with r_b being defined in the inset, which increases with decreasing $\hat{\ell}$ and is smaller near the critical line.

smaller near the critical line. In fact, $r_b \cong 0.2a$ at the transition for $\hat{s} = -1.4$.

The transition surface is determined from minimization of Ω or maximization of $\mathcal{G}$ from Eq. (3.22). In the left panels of Fig. 11, we plot $\mathcal{G}$ and $\hat{\ell}^2\mathcal{F}$ vs $\hat{\ell}$ for $(\hat{t},\hat{s}) = (-8, -1.31)$. The curve of $\mathcal{F}$ from the Derjaguin approximation nicely agrees with that from Eq. (3.2) for $\hat{\ell} \lesssim 0.6$. For this $(\hat{t},\hat{s})$, we find two stationary solutions satisfying Eqs. (3.1) and (3.5) in a window range $(0.96 < \hat{\ell} < 1.08$ for this example). Outside this range, one solution becomes unstable and the other one remains as a stable solution. In the bistable range, $\mathcal{G}$ is larger on the equilibrium branch and smaller on the metastable one, so the transition is at the cross-point of the two branches of $\mathcal{G}$.

In Fig. 11 the slope of $\mathcal{G}$ is very steep with bridging. It is -37.8 at the transition, where $\hat{\ell} = 1.04 \gg \xi/a = 0.09$. It is further amplified for smaller $\hat{\ell}$ and is -76.6 at $\hat{\ell} = 0.08 \cong \xi/a$. Here, for $\ell \gg \xi$, a well-defined bridging domain exists, and $\mathcal{G}$ changes with a change of its surface area. In fact, use of the surface tension σ in Eq. (2.12) gives $2\pi a^2\sigma/k_B T_c = 57.9$ at $\hat{t} = -8$. Thus, with a well-defined bridge, Eq. (3.25) yields the capillary force [4,32],

$$\mathcal{F} \sim 2\pi a^2\sigma/k_B T_c \sim (a/\xi)^2. \tag{4.3}$$

This relation is valid for $\ell \gtrsim \xi$. For smaller $\ell \lesssim \xi$, the growth $(\sim\hat{\ell}^{-2})$ in Eq. (3.26) becomes dominant. These features will be further examined in Figs. 12, 13, and 16.

In the original units, the force with a well-defined bridge is of order $k_B T_c a/\xi^2$, which increases as we move away

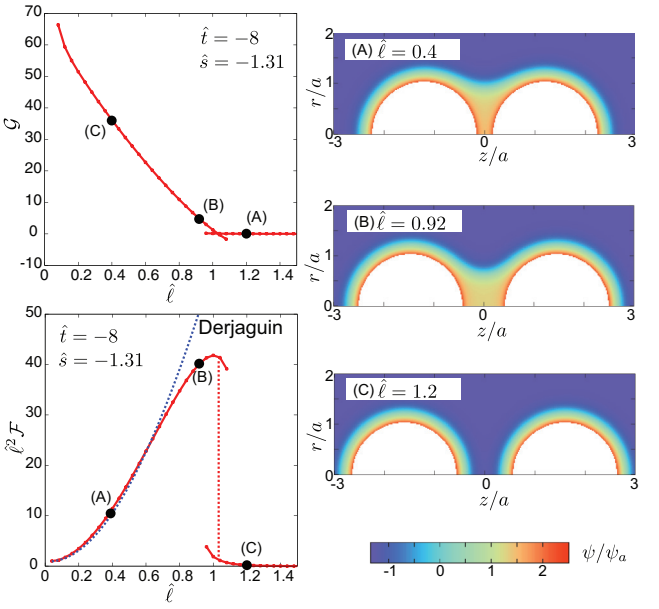

FIG. 11. (Color online) Left: $\mathcal{G}$ (top) and $\hat{\ell}^2\mathcal{F}$ (bottom) vs $\hat{\ell}$ for $(\hat{t},\hat{s}) = (-8, -1.31)$ across the bridging transition surface. There appear two branches of stationary solutions in a window range $(0.96 < \hat{\ell} < 1.08)$. Maximization of $\mathcal{G}$ determines the equilibrium state. For $\mathcal{F}$, a curve from the Derjaguin approximation (blue dotted line) nicely agrees with that from Eq. (3.25). Right: $\psi(r,z)/\psi_a$ in the z-r plane $(r = (x^2 + y^2)^{1/2})$ with the same $(\hat{t},\hat{s})$ according to the color bar, where $(\hat{\ell}, \psi(0,0)/\psi_a) =$ (A) (0.4,1.48), (B) (0.92,1.28), and (C) (1.2, −1.23) from above. The corresponding points are marked in the left.

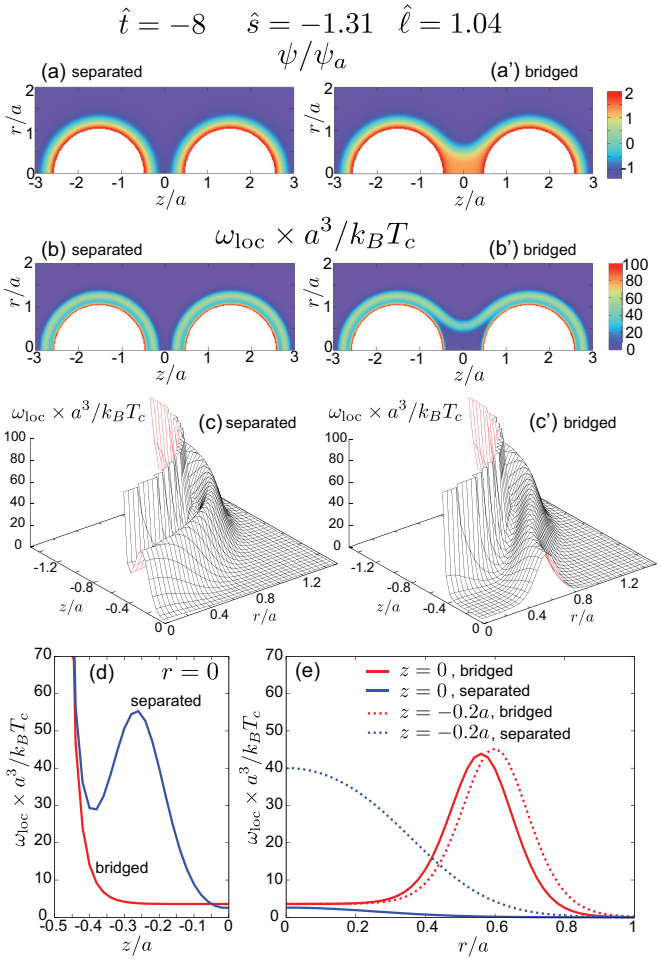

FIG. 12. (Color online) Separated state (left) and bridged state (right) at a first-order transition point with $(\hat{t},\hat{s},\hat{\ell}) = (-8, -1.31, 1.04)$. Here ψ/ψ_a in (a) and (a′) and $\omega_{\rm loc}a^3/k_BT_c$ in (b) and (b′) are written in gradation according to the color bars. Also $\omega_{\rm loc}a^3/k_BT_c$ is diplayed in bird's eye views for $z \leqslant 0$ in (c) and (c′), along the z axis on the line $r = 0$ in (d), and as a function of r/a at $z = 0$ and $-0.2a$ in (e).

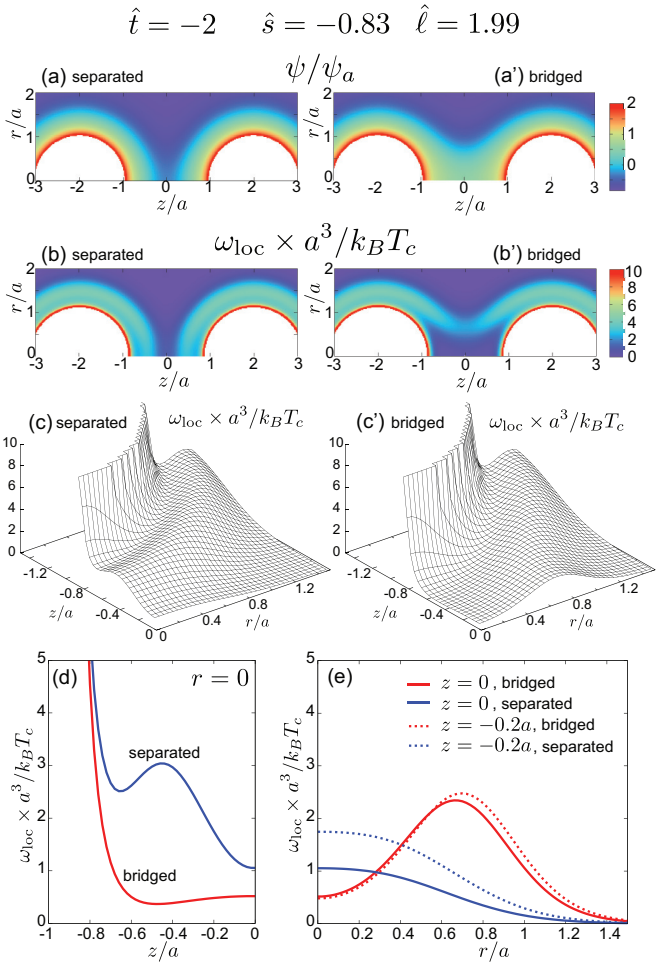

FIG. 13. (Color online) Separated state (left) and bridged state (right) at a first-order transition point near the bulk criticality with $(\hat{t},\hat{s},\hat{\ell}) = (-2, -0.83, 1.99)$, where ψ/ψ_a in (a) and (a′) and $\omega_{\rm loc}a^3/k_BT_c$ in (b) and (b′). Also $\omega_{\rm loc}a^3/k_BT_c$ is displayed in a bird's eye views in (c) and (c′) for $z \leqslant 0$, along the z axis on the line $r = 0$ in (d), and as a function of r/a at $z = 0$ and $-0.2a$ in (e).

from the bulk criticality. Also in Fig. 14, we shall see that $\mathcal{F}$ increases with lowering τ, where bridging occurs continuously. However, the exponential tail of the interaction in Eq. (3.28) in separated states ($\propto e^{-\ell/\xi}$) increases as the bulk criticality is approached, which was indeed observed experimentally [17].

In the right panels of Fig. 11, we display $\psi(r,z)/\psi_a$ in the plane of $r = (x^2 + y^2)^{1/2}$ and z in two bridged and one separated states at different $\hat{\ell}$. We can see that the bridging radius r_b is larger in (a) (far below the bridging transition) than in (b) (close to it). The midplane between the two particles is filled with the phase outside the particles in (c) in a separated state.

In these phase diagrams the lowest value of $\hat{t}$ is -10. With further lowering $\hat{t}$, there is still a tendency of decreasing $\hat{\ell}_{\rm cx}$ and $\hat{\ell}_c$. For example, for $\hat{t} = -20$, we find $\hat{\ell}_{\rm cx} = 0.69$ on CX and $(\hat{\ell},\hat{s}) = (\hat{\ell}_c,\hat{s}_c) = (0.395, -2.0)$ at the corresponding bridging critical point.

B. Profiles at transition and critical points

In Figs. 12 and 13, we compare the profiles of $\psi(r,z)$ and $\omega_{\rm loc}(r,z)$ in separated and bridged states at two typical transition points on the bridging transition surface in Fig. 8. That is, $(\hat{t},\hat{s},\hat{\ell})$ is $(-8, -1.31, 1.04)$ in Fig. 12 and $(-2, -0.83, 1.99)$ in Fig. 13. These points correspond to points (A) and (B) in Fig. 9. The former in Fig. 12 is relatively far from the bulk criticality with $\xi/a \cong 0.09$, and the interface is wel-defined. The latter in Fig. 13 is closer to it with $\xi/a \cong 0.19$, and the interface is broadened and the separation is widened to $\hat{\ell} = 1.99$.

More remarks on Figs. 12 and 13 are as follows: (1) The profiles of ψ/ψ_a are distinctly different in the separated and bridged states. Its midpoint value is 1.27 in (a) and -1.07 in (a′) in Fig. 12, while it is 0.54 in (a) and -0.31 in (a′) in Fig. 13. (2) We can see layer regions with a peak in $\omega_{\rm loc}a^3/k_BT_c$, which enclose the colloid surfaces at a distance of order $\xi_{\rm ad}$ in Eq. (3.19) except for the bridged surface regions. See Fig. 1 for the profile of $\hat{s} = -1.31$ around a single particle. These layers around the two spheres are separated in (b), while

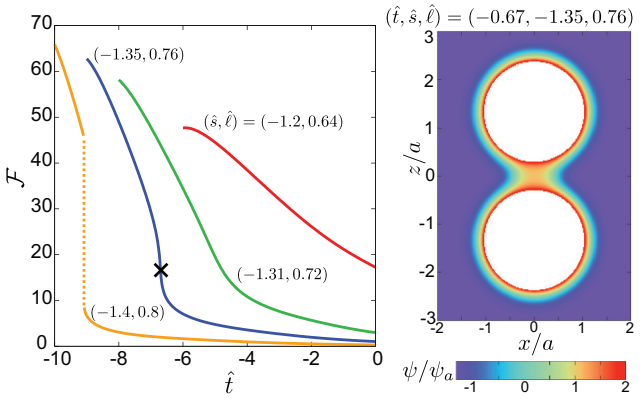

FIG. 14. (Color online) Left: $\mathcal{F}$ vs $\hat{t}$ for $(\hat{s},\hat{\ell}) = (-1.2,0.64)$, $(-1.31,0.72)$, $(-1.35,0.76)$, and $(-1.4,0.8)$ from right. The slope $\partial\mathcal{F}/\partial\hat{t}$ becomes steeper near the bridging critical line. On the third curve (from right), a critical point ($\times$) is passed. On the fourth curve, a jump due to a bridging transition appears. Right: $\psi(x,0,z)/\psi_a$ on the xz plane according to the colored bar at a critical point $(\hat{t},\hat{s},\hat{\ell}) = (-0.67,-1.35,0.76)$ ($\times$ in the left panel). It is equal to 1.08 at the center $x = z = 0$.

they are detached from the colloid surfaces in the bridged parts in (b′). (3) We also display $\omega_{\rm loc}a^3/k_BT_c$ in bird's eye views in (c) and (c′), Comparing them, we recognize how a discontinuous change occurs with the total grand potential unchanged. (4) In the bottom plates, we plot one-dimensional profiles of $\omega_{\rm loc}a^3/k_BT_c$ in the two states. They are presented along the z axis at $r = 0$ in (d) and along the r axis at $z = 0$ and $-0.2a$ in (e). Note that the integral $\int_0^\infty dr r\omega_{\rm loc}a/k_BT_c$ is equal to $\mathcal{F}/2\pi$ from Eq. (3.25) and is of order $r_b a\sigma$ with σ being the surface tension.

Figures 12 and 13 demonstrate that there should be a balance between the free energy cost of creating a bridge ($\sim\pi\sigma\ell r_b$) and the free energy decrease on the colloid surfaces ($\sim -\pi\sigma r_b^2$) at the transition [see (d) and (e)]. The origin of the latter is evident from comparison of the two curves of $\hat{s} = \pm 1.31$ in Fig. 1. Also in Fig. 13, we have $\mathcal{F} = 6.79$ with bridging and $2\pi a^2\sigma/k_BT_c = 10.09$, in agreement with Eq. (4.3). The corresponding values in Fig. 12 have already been given above Eq. (4.3).

We also examine the behavior of $\mathcal{F}$ and the profile of ψ near the critical line. In Fig. 14 we plot $\mathcal{F}$ vs $\hat{t}$ for four sets of $(\hat{s},\hat{\ell})$. Here the force $\mathcal{F}$ increases with lowering $\hat{t} < 0$. The right two curves are in regions with $\ell < \ell_c$ in Fig. 8, and there is no discontinuous change (as in Fig. 17). The third curve meets a critical point $(\hat{t},\hat{s},\hat{\ell}) = (-0.67,-1.35,0.76)$. On these curves, bridging is achieved continuously as $\hat{t}$ is lowered. The fourth curve passes through the bridging transition surface and exhibits a discontinuous change. The slope $\partial\mathcal{F}/\partial\hat{t}$ becomes steep near the critical line and diverges on it.

C. Overall behaviors

In Fig. 15 we plot $\mathcal{G}$, $\mathcal{F}$, and the normalized excess adsorption $(\Gamma - \Gamma_\infty)/a^3\psi_a$ vs $\hat{\ell}$ at $\hat{t} = -8$ for six values of $\hat{s}$. Here Γ is the adsorption in Eq. (3.18) and Γ_∞ is its value for large separation. With varying $\hat{\ell}$, a discontinuous bridging transition occurs for $\hat{s} = -1.31$, -1.35, and -1.4, while there is no discontinuity for $\hat{s} = -1.43$, -1.5, and -1.6. In the

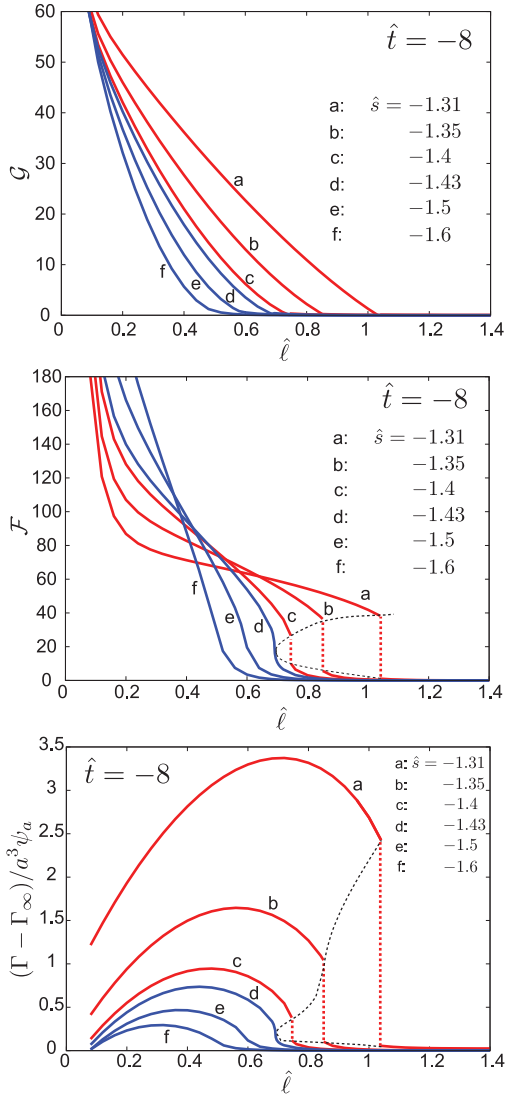

FIG. 15. (Color online) $\mathcal{G}$ (top), $\mathcal{F}$ (middle), and normalized excess adsorption $(\Gamma - \Gamma_\infty)/a^3\psi_a$ (bottom) vs $\hat{\ell}$ for $\hat{t} = -8$, where $\hat{s}$ is (a)-1.31, (b)-1.35, (c)-1.4, (d)-1.43, (e)-1.5, and (f)-1.6. For (a), (b), and (c), a discontinuous bridging transition occurs at $\hat{\ell} = 1.04$, 0.85, and 0.745, respectively. For (d), (e), and (f), the curves are continuous in the whole range of $\hat{\ell}$, where $\Gamma - \Gamma_0$ becomes negative for $\hat{\ell} < 0.08$ (not shown). For (d) the curve nearly passes through a critical point, where $-\partial\mathcal{F}/\partial\hat{\ell}$ and $-(\partial\Gamma/\partial\hat{\ell})/a^3\psi_a$ are very large.

latter, $\Gamma - \Gamma_0$ becomes negative for $\hat{\ell} < 0.08$ (not shown). For $\hat{s} = -1.43$ [the curves (d)], a critical point is nearly passed, where we have very steep slopes: $\partial\mathcal{F}/\partial\hat{\ell} = -3413$ and $(\partial\Gamma/\partial\hat{\ell})/a^3\psi_a = -39.5$. This behavior indicates divergence of $\partial\mathcal{F}/\partial\hat{\ell}$ and $\partial\Gamma/\partial\hat{\ell}$ on the bridging critical line. In addition, the curves of $(\Gamma - \Gamma_\infty)/a^3\psi_a$ vs $\hat{\ell}$ exhibit rounded maxima at an intermediate $\hat{\ell}$. This behavior can be understood from the right panel of Fig. 10, where the bridging radius r_b increases with decreasing $\hat{\ell}$.

In Fig. 15 the formula (4.3) for bridged states holds for $\hat{\ell} \gtrsim \xi/a = 0.09$. For smaller $\hat{\ell}$, $\mathcal{F}$ diverges as in Eq. (3.26). In Fig. 16 we thus plot $\psi(r,0)/\psi_a$ and $r\omega_{\rm loc}(r,0) \times 2\pi a^2/k_BT_c$ as functions of r/a at $z = 0$ in the midplane at

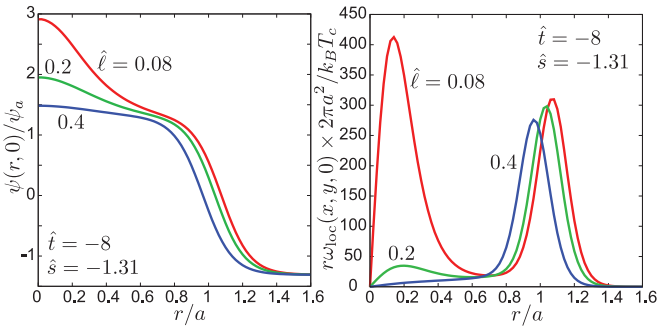

FIG. 16. (Color online) Midplane profiles: $\psi(r,0)/\psi_a$ (left) and $r\omega_{\rm loc}(r,0) \times 2\pi a^2/k_BT_c$ (right) vs r/a at $z = 0$ for $(\hat{t},\hat{s}) = (-8, -1.31)$. Area below each curve (right) gives $\mathcal{F}$. Here $\hat{\ell} = 0.4$, 0.2, and 0.08, for which $\mathcal{F} = 71.7$, 87.4, and 185, respectively. At $r \sim a$, a well-defined interface exists. In the center region, ψ and $\omega_{\rm loc}$ grow for $\hat{\ell} \lesssim \xi/a = 0.09$.

$(\hat{t},\hat{s}) = (-8, -1.31)$ for $\hat{\ell} = 0.4$,0.2, and 0.08. We recognize growing of ψ and $\omega_{\rm loc}$ on the midplane with decreasing $\hat{\ell} \lesssim \xi/a$.

We also examine how a continuous changeover between bridged and separated states is achieved for small $\hat{\ell} < \hat{\ell}_c(\hat{t})$. This case has been mentioned in the explanation of Fig. 10. In Fig. 17 we display $\psi(r,0)/\psi_a$ and $r\omega_{\rm loc}(r,0) \times 2\pi a^2/k_BT_c$ vs r/a at $z = 0$ for $\hat{t} = -8$ and $\hat{\ell} = 0.5$. Here $\hat{s}$ is decreased from a value close to CX, -1.31, to smaller values away from CX. The profile of $\psi(r,0)/\psi_a$ at $\hat{s} = -1.31$ indicates the presence of a well-defined interface with a thickness of order ξ. However, with decreasing $\hat{s}$ from -1.31 to -1.7, the profile of $\psi(r,0)/\psi_a$ is gradually broadened and $\mathcal{F}$ decreases from 67.7 to 13.8.

D. Stability of separation distance

In Figs. 14 and 15, the derivatives $\partial\mathcal{F}/\partial\hat{\ell}(\propto \partial^2\Omega/\partial\ell^2)$ and $\partial\mathcal{F}/\partial\hat{t}(\propto \partial^2\Omega/\partial\ell\partial\tau)$ are negative and tend to diverge as the bridging critical line is approached. We mention one implication of this singular behavior.

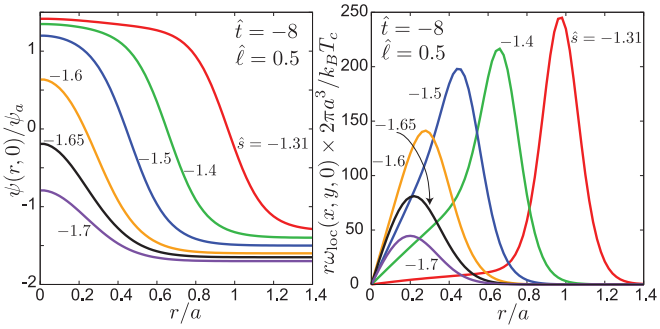

FIG. 17. (Color online) Midplane profiles: $\psi(r,0)/\psi_a$ (left) and $r\omega_{\rm loc}(r,0) \times 2\pi a^2/k_BT_c$ (right) vs r/a at $z = 0$ for $(\hat{t},\hat{\ell}) = (-8,0.5)$. Area below each curve (right) gives $\mathcal{F}$. Here $\hat{s}$ is varied as -1.31, -1.4, -1.5, -1.6, -1.65, and -1.7, for which $\mathcal{F}$ is equal to 67.7, 76.8, 65.4, 40.1, 25.8, and 13.8, respectively. In this case, $\hat{\ell} < \hat{\ell}_c$ holds, so changeover between bridged and separated states is continuous.

In this paper we have been fixing the colloid separation ℓ at a constant. To achieve this constraint, let us suppose the presence of an externally applied potential $U_{\rm ext}(\ell)$ between two colloidal particles [4]. For example, optical tweezers have been used to trap colloidal particles at small separation [17,51]. In equilibrium, we should minimize the sum $\Omega(\ell) + U_{\rm ext}(\ell)$ with respect to ℓ. Then, the equilibrium separation ℓ is determined from

$$F_{\rm ext} = -\frac{\partial}{\partial\ell}U_{\rm ext} = \frac{1}{a}k_BT_c\mathcal{F}. \tag{4.4}$$

In order to ensure the stability of this equilibrium separation ℓ, we need to require

$$K_{\rm ext} = \frac{\partial^2}{\partial\ell^2}U_{\rm ext} > \frac{1}{a^2}k_BT_c\left(-\frac{\partial\mathcal{F}}{\partial\hat{\ell}}\right), \tag{4.5}$$

where $K_{\rm ext}(\ell)$ is the spring constant of the externally applied potential. The thermal fluctuation of the separation ℓ is increased with decreasing the effective spring constant $K_{\rm eff} = K_{\rm ext} + (k_BT_c/a^2)\partial\mathcal{F}/\partial\hat{\ell}$ while $K_{\rm eff} > 0$. Moreover, there is a possibility of violation of the inequality (4.5) or negativity of $K_{\rm eff}$ sufficiently close to the bridging critical line, where the colloid configuration determined from Eq. (4.4) is unstable.

V. SUMMARY AND REMARKS

We have investigated the adsorption-induced interaction between two neutral colloidal particles with common radius a in a near-critical binary mixture. Use has been made of our local functional theory [30]. In the strong adsorption limit, we have calculated the normalized free energy deviation $\mathcal{G}$ (with minus sign) and the normalized force $\mathcal{F}$ as universal functions of scaled reduced temperature $\hat{t} = \tau/\tau_a$ (where $\tau_a = (\xi_0/a)^{1/\nu}$), scaled reservoir order parameter $\hat{s} = \psi_\infty/\psi_a$ (where $\psi_a \sim \tau_a^\beta$), and scaled separation distance $\hat{\ell} = \ell/a$.

Main results are as follows:

(1) We have expressed the forces for many colloidal particles in Eq. (3.6) and the force between two neutral colloidal particles in Eq. (3.25) using the stress tensor due to the order parameter deviation. Some general discussions on this aspect are given in Appendix A. Generalization including charges will be presented in another paper.

(2) The interaction is much enhanced for $\hat{s} < 0$ as in Figs. 3–7, where the component favored by the colloid surfaces is poor in the reservoir and the order parameter disturbances around the surfaces are large as in Fig. 1. It is 10–100 times larger than at the bulk criticality.

(3) The Derjaguin approximation [3,4] can be made on the force $\mathcal{F}$ for $\hat{\ell} \lesssim 1$ on the basis of the results for films in our previous paper [30], as discussed in Appendix B. It cannot describe the bridging transition, but it predicts the short separation growth in Eq. (3.27) and the exponential decay for large $\hat{\ell}$ in Eq. (3.28). These results agree with the calculations from Eq. (3.25) for $\hat{\ell} \lesssim 1$.

(4) We have compared the van der Waals interaction and the adsorption-induced interactions. The former may be neglected at off-critical compositions and particularly at a bridging transition even for typical values of the Hamaker constant $A_{\rm H}(\sim 10^{-19}{\rm J})$, as shown in Fig. 7.

(5) We have found a surface of a first-order bridging transition $\hat{\ell} = \hat{\ell}_{\rm cx}(\hat{t},\hat{s})$ in the $\hat{t}$-$\hat{s}$-$\hat{\ell}$ space in Fig. 8, across which a discontinuous change occurs between separated and bridged states. This surface starts from the bulk coexistence surface and ends at a bridging critical line $\hat{\ell} = \hat{\ell}_c(\hat{t})$. The discontinuity vanishes and the derivatives of the force with respect to T and ℓ diverge on the critical line as in Figs. 14 and 15. The critical separation $\hat{\ell}_c$ decreases with decreasing $\hat{t}$, which assumes the maximum 2.6 at $\hat{t} = -1.0$ and is 0.395 at $\hat{t} = -20$.

(6) We have calculated $\mathcal{G}$, $\mathcal{F}$, and the excess adsorption $\Gamma - \Gamma_\infty$ for various parameters in Fig. 15. With a well-defined bridging domain with $\ell \gtrsim \xi$, $\mathcal{F}$ is given by the capillary force proportional to the surface tension σ in Eq. (4.3). For $\ell \lesssim \xi$, $\mathcal{F}$ grows as $\hat{\ell}^{-2}$ in accord with the de Gennes-Fisher theory.

(7) We have changed $\hat{s}$ (or $\hat{t}$) away from the bulk coexistence surface fixing $\hat{\ell}$ below $\hat{\ell}_c$ in Sec. IV C. There, we have found continuous changeover between bridged and separated states as in Figs. 14 and 16.

(8) We have pointed out a possibility of an instability of the colloid separation distance near the bridging critical line where $\partial\mathcal{F}/\partial\hat{\ell}$ diverges.

We give some remarks below:

(1) To measure the force between colloidal particles, the geometry of a sphere and a plate has mostly been used [17,36], while the geometry of two spheres was also used in a liquid crystal solvent [51]. In these two geometries, we expect essentially the same theoretical results for near-critical fluids. Systematic experiments on the force and the bridge formation at off-critical compositions near the bulk criticality should be promising.

(2) There can arise repulsion between solid objects with asymmetric boundary conditions (with different signs of h_1) [18,26,27]. The adsorption-induced interaction in such asymmetric conditions should also be studied.

(3) Real colloidal particles are usually charged and the charge effect can be crucial [7–10,17]. For example, between a sphere and a plate, Hertlein *et al.* [17] measured the adsorption-induced attractive interaction for $\ell \gtrsim 0.1\,\mu$m with $a = 1.85\,\mu$m for various τ at the critical composition. In their experiment, the screened Coulomb interaction was dominant for smaller ℓ and decayed exponentially ($\propto e^{-\kappa\ell}$) with salt, where the screening length κ^{-1} (=12 nm) was shorter than ℓ measured.

(4) The degree of ionization depends on the surface values of the composition and the ion densities. In aqueous fluids, the colloid surface can be hydrophobic for weak ionization and hydrophilic with progress of ionization [7,8,22]. Furthermore, added salts act as selective impurities to cause precipitation forming a wetting layer on the surfaces [16,22]. Aggregation of colloids could depend on these elements also.

(5) The colloidal particles themselves act as selective impurities in a mixture solvent [16], where the selectivity can be strong due to their large surface area [46]. Flocculation could be understood as phase separation in such three-component systems [7–12,15].

(6) In dynamics of bridging and aggregation of colloidal particles, the hydrodynamic flow should be crucial [31,38]. The dynamical aspects have not yet been fully studied experimentally. Simulations on the dynamics of charged colloids are complicated, where we need to integrate the dynamic equations for the composition, the ions, and the colloidal particles [31,42].

(7) We should examine the nanobubble bridging in water [37]. From our viewpoint, nanobubbles appear with addition of hydrophobic impurities in water [16]. Here dynamics of bubble formation and disruption upon a pressure or temperature change is of great interest [38].

ACKNOWLEDGMENTS

We would like to thank Daniel Beysens for valuable discussions, This work was supported by Grant-in-Aid for Scientific Research from the Ministry of Education, Culture, Sports, Science and Technology of Japan.

APPENDIX A: ADSORPTION-INDUCED FORCE BETWEEN COLLOIDAL PARTICLES IN TERMS OF STRESS TENSOR

We consider two configurations of colloid particles in a near-critical fluid. That is, the colloid centers are at $\boldsymbol{R}_\alpha$ in one configuration and at $\boldsymbol{R}_\alpha + \delta\boldsymbol{R}_\alpha$ in another slightly displaced one ($\alpha = 1,2,\dots$). In these two states, we write the profiles of ψ as $\psi(\boldsymbol{r})$ and $\psi'(\boldsymbol{r}')$ using different symbols. The space positions are written as $\boldsymbol{r}$ and $\boldsymbol{r}'$, respectively. We are interested in the difference between the grand potentials, $\Omega = \Omega(\{\boldsymbol{R}_\alpha\})$ and $\Omega' = \Omega(\{\boldsymbol{R}_\alpha + \delta\boldsymbol{R}_\alpha\})$, for these two states. From Eqs. (3.2) and (3.3), the grand potential Ω' for $\psi'(\boldsymbol{r}')$ is written as

$$\frac{\Omega'}{k_B T_c} = \int' d\boldsymbol{r}' \left[\hat{\omega}(\psi') + \frac{C(\psi')}{2}|\nabla'\psi'|^2\right] - \int dS' h_1 \psi', \tag{A1}$$

where $\psi' = \psi'(\boldsymbol{r}')$, $\nabla' = \partial/\partial\boldsymbol{r}'$, and

$$\hat{\omega}(\psi) = [f(\psi) - f_\infty - \mu_\infty(\psi - \psi_\infty)]/k_B T_c. \tag{A2}$$

The $\int' d\boldsymbol{r}'$ is the integral outside the displaced colloidal particle, while $\int dS'$ is that on their spherical surfaces. We assume $\psi \to \psi_\infty$ far from the colloidal particles.

As a mathematical technique, we assume a mapping relation between the positions $\boldsymbol{r}'$ and $\boldsymbol{r}$ as

$$\boldsymbol{r}' = \boldsymbol{r} + \boldsymbol{u}(\boldsymbol{r}), \tag{A3}$$

where $\boldsymbol{u}$ is a *displacement* vector vanishing far from the colloidal particles. Its surface value on the αth colloid particle is given by $\delta\boldsymbol{R}_\alpha$. We rewrite the right-hand side of Eq. (A1) by changing $\boldsymbol{r}' = (x',y',z') = (x_1',x_2',x_3')$ to $\boldsymbol{r} = (x,y,z) = (x_1,x_2,x_3)$. To first order in $\boldsymbol{u}$, we may set $d\boldsymbol{r}' = d\boldsymbol{r}(1 + \nabla\cdot\boldsymbol{u})$ and $\partial/\partial x_i' = \partial/\partial x_i - \sum_j D_{ij}\partial/\partial x_j$, where D_{ij} is the strain tensor,

$$D_{ij} = \partial u_j/\partial x_i. \tag{A4}$$

The deviation of the order parameter is written as

$$\delta\psi(\boldsymbol{r}) = \psi'(\boldsymbol{r}') - \psi(\boldsymbol{r}). \tag{A5}$$

To first order in $\boldsymbol{u}$ and $\delta\psi$, we calculate $\delta\Omega = \Omega' - \Omega$ as

$$\frac{\delta\Omega}{k_B T_c} = \int d\boldsymbol{r}\Big[\Big(\hat{\omega} + \frac{C}{2}|\nabla\psi|^2\Big)\nabla\cdot\boldsymbol{u} + \Big(\frac{\partial\hat{\omega}}{\partial\psi} + \frac{C'}{2}|\nabla\psi|^2\Big)\delta\psi + C\nabla\psi\cdot\nabla\delta\psi - C\sum_{ij} D_{ij}\nabla_i\psi\nabla_j\psi\Big] - \int dS h_1\delta\psi, \tag{A6}$$

where $C' = \partial C/\partial\phi$, $\nabla_i = \partial/\partial x_i$, and $\int d\boldsymbol{r}$ is the integral outside the colloidal particles at the original colloid positions, and $\int dS$ is that on their surfaces. Using $\Pi_{\psi ij}$ in Eq. (3.7), Π_∞ in Eq. (3.9), and $\delta\Omega/\delta\psi = \delta F_b/\delta\psi - \mu_\infty$ [see Eq. (3.5)], we simplify Eq. (A6) as

$$\delta\Omega = \int d\boldsymbol{r}\sum_{ij}(\Pi_\infty\delta_{ij} - \Pi_{\psi ij})D_{ij} + \int d\boldsymbol{r}\frac{\delta\Omega}{\delta\psi}\delta\psi - k_B T_c\int dS[C\boldsymbol{n}\cdot\nabla\psi + h_1]\delta\psi. \tag{A7}$$

This relation is general and valid even in nonequilibrium.

In this paper, we assume that the original state is in equilibrium. That is, we assume the equilibrium relations (3.1) and (3.5) for $\psi(\boldsymbol{r})$. Then only the first term remains in Eq. (A7). Further using the equilibrium relation $\sum_j \nabla_j \Pi_{\psi ij} = 0$ in the fluid and $\boldsymbol{u} = \delta\boldsymbol{R}_\alpha$ on the surface of the αth colloidal particle, we may rewrite Eq. (A7) as

$$\delta\Omega = \sum_\alpha\int_\alpha dS\sum_{ij}(\Pi_{ij} - \Pi_\infty\delta_{ij})n_{\alpha i}\delta R_{\alpha j}, \tag{A8}$$

where $\int_\alpha dS$ is the integral on the surface of the αth colloidal particle and $\boldsymbol{n}_\alpha = (n_{\alpha x}, n_{\alpha y}, n_{\alpha z})$ is the normal unit vector. This yields Eq. (3.6).

In the equilibrium case of two colloidal particles in Fig. 2, we set $\delta\boldsymbol{R}_1 = \delta\ell\boldsymbol{e}_z$ and $\delta\boldsymbol{R}_2 = 0$, where $\boldsymbol{e}_z$ is the unit vector along the z axis. From Eq. (A8), $\partial\Omega/\partial\ell = \lim_{\delta\ell\to 0}\delta\Omega/\delta\ell$ is obtained as

$$\frac{\partial\Omega}{\partial\ell} = \int_1 dS\sum_i(\Pi_{iz} - \Pi_\infty\delta_{iz})n_{1i}, \tag{A9}$$

where the surface integral is on the surface of the first colloidal particle. However, the above formula is not suitable for numerical calculations in the strong adsorption case. To devise a more convenient one, we integrate the equilibrium equation $\sum_j \nabla_j \Pi_{zj} = 0$ in the fluid region bounded by the upper colloid surface, a semisphere surface $S_{\rm semi}$, and a circular surface $S_{\rm mid}$ (see Fig. 1), where the latter surfaces are represented by

$$S_{\rm semi} = \{(x,y,z)|z > 0, x^2 + y^2 + z^2 = L^2\},\quad S_{\rm mid} = \{(x,y,z)|z = 0, x^2 + y^2 = L^2\}. \tag{A10}$$

Then $\partial\Omega/\partial\ell$ in Eq. (A9) is equal to the sum of the surface integrals on $S_{\rm mid}$ and $S_{\rm semi}$. In the limit of large L, the integral on $S_{\rm semi}$ vanishes and that on $S_{\rm mid}$ yields Eq. (3.25). Here, from the geometrical symmetry, $\partial\psi/\partial z = 0$ on the midplane, and $\Pi_{\psi zz} = \Pi_\infty - \omega_{\rm loc}$ follows from Eq. (3.10).

APPENDIX B: DERJAGUIN APPROXIMATION

The Derjaguin approximation [3] simply relates the interaction free energy between two colloidal particles for small separation to that between two plates. We here apply this method to our problem.

We write the grand potential for a film with thickness D as $\Omega_{\rm f}(D)$ (per unit area). If the two spheres are separated without bridging, the corresponding film is in separated states for $D > \ell$. Thus,

$$\Omega(\ell) - \Omega_\infty \cong \pi a\int_\ell^\infty dD[\Omega_{\rm f}(D) - \Omega_{\rm f\infty}]. \tag{B1}$$

Here $\Omega_{\rm f\infty}$ is the limit of $\Omega_{\rm f}(D)$ for large D, where $\psi_m = \psi(D/2) \cong \psi_\infty$ [30]. From Eq. (B1) the force is given by

$$\frac{\partial}{\partial\ell}\Omega(\ell) \cong -\pi a[\Omega_{\rm f}(\ell) - \Omega_{\rm f\infty}]. \tag{B2}$$

On the other hand, if the two spheres are bridged, the corresponding film state changes from a condensed state (with $\psi_m = \psi(D/2) > 0$) to separated ones (with $\psi_m \sim \psi_\infty < 0$) with increasing D. Thus, the formula (B1) is not well justified in bridged states, but in our analysis the formula (B2) produced $\mathcal{F}$ close to that from Eq. (3.25) for $\ell \lesssim a$ in both separated and bridged states (see Fig. 11).

For Ising-like near-critical systems, $\Omega_{\rm f}(D)$ is expressed in the de Gennes-Fisher scaling form [23,24] as

$$\Omega_{\rm f}(D) = \Omega_{\rm f\infty} - k_B T_c D^{-2}\Delta(t,s), \tag{B3}$$

in three dimensions. In our previous paper [30], we calculated $\Delta(t,s)$ in the strong adsorption limit as a universal function of two scaling parameters t and s defined by

$$t = \tau(D/\xi_0)^{1/\nu}, \tag{B4}$$

$$s = \psi_\infty/\psi_D, \tag{B5}$$

where $\psi_D = 1.47 b_{\rm cx}(\xi_0/D)^{\beta/\nu}$. If D is replaced by a, we obtain $\hat{t}$ and $\hat{s}$ in Eqs. (3.12) and (3.13). For small t and s, $\Delta(t,s)$ approaches its critical-point value $\Delta_{\rm cri}$ ($\cong 0.279$ in our theory [30]). We also introduce the normalized force density $\mathcal{A}(t,s)$ between the plates by

$$\frac{\partial}{\partial D}\Omega_{\rm f}(D) = k_B T D^{-3}\mathcal{A}(t,s). \tag{B6}$$

From Eqs. (B3) and (B6), Δ and $\mathcal{A}$ are related by

$$\mathcal{A}(t,s) = \Big[2 - \frac{\beta s}{\nu}\frac{\partial}{\partial s} - \frac{t}{\nu}\frac{\partial}{\partial t}\Big]\Delta(t,s). \tag{B7}$$

From our previous work [30], Δ and $\mathcal{A}$ behave as follows. (1) Near the bulk critical point, they tend to $\Delta_{\rm cri} \sim 0.25$ and $\mathcal{A}_{\rm cri} = 2\Delta_{\rm cri}$, respectively. (2) Just below the capillary condensation line $s = s_{\rm tr}^{\rm ca}(t)$, we have $\Delta \lesssim 1$ and $\mathcal{A} \gg 1$, where $\mathcal{A} \cong 2|t|^{2\nu}$ for $|t| \gg 1$ [31]. (3) On approaching the negative branch of CX or as $s \to -s_{\rm cx} = -0.68|t|^{2\nu}$, Δ grows (up to of order $|t|^{2\nu}$ for $|t| \gg 1$) and $\mathcal{A}$ decreases (down to of order $|t|^{3\nu}e^{-D/\xi}$ for $|t| \gg 1$) [52] (see Figs. 12 and 16 of Ref. [30]).

From Eqs. (3.22) and (B2) $\mathcal{F}$ is now expressed as

$$\mathcal{F}(\hat{\ell}) \cong \pi\hat{\ell}^{-2}\Delta(t_\ell, s_\ell). \tag{B8}$$

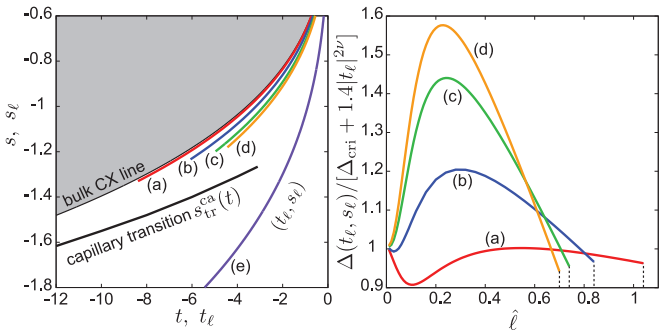

FIG. 18. (Color online) Left: Trajectories (t_ℓ,s_ℓ) in Eqs. (B9) and (B10) at $\hat{t}=-8$ with $\hat{s}$ being (a) -1.31, (b) -1.35, (c) -1.4, (d) -1.43, and (e) -2.04. Curves of (a)–(d) are written for $\hat{\ell}<\hat{\ell}_{tr}$ in bridged states, while on curve (e) separated states are realized for any $\hat{\ell}$. These curves approach the bulk critical point as $\hat{\ell}\to 0$. Displayed also are the capillary condensation line $s=s_{tr}^{ca}(t)$ and the bulk coexistence curve $s=-s_{cx}(t)$ (negative branch). Right: $\Delta(t_\ell,s_\ell)$ divided by $\Delta_{cri}+1.4|t_\ell|^{2\nu}$ vs $\hat{\ell}(<\hat{\ell}_{cx})$ for curves (a)–(d) [see Eq. (B13)].

Replacing D in t and s in Eq. (B4) by ℓ, we introduce

$$t_\ell=\hat{t}\hat{\ell}^{1/\nu}=\tau(\ell/\xi_0)^{1/\nu}, \tag{B9}$$

$$s_\ell=\hat{s}\hat{\ell}^{\beta/\nu}=\psi_\infty/\psi_\ell, \tag{B10}$$

with $\psi_\ell=1.47b_{cx}(\xi_0/\ell)^{\beta/\nu}$. Differentiation of $\mathcal{F}$ in Eq. (B8) with respect to $\hat{\ell}$ at fixed $\hat{t}$ and $\hat{s}$ yields

$$\frac{\partial}{\partial\hat{\ell}}\mathcal{F}(\hat{\ell})\cong-\pi\hat{\ell}^{-3}\mathcal{A}(t_\ell,s_\ell). \tag{B11}$$

Now we have the three sets of the parameters, $(\hat{t},\hat{s})$ in Eqs. (3.12) and (3.13), (t,s) in Eqs. (B4) and (B5), and (t_ℓ,s_ℓ) in Eqs. (B9) and (B10). Notice that the following combinations are independent of a, D, and ℓ:

$$q\equiv\hat{s}/|\hat{t}|^\beta=s/|t|^\beta=s_\ell/|t_\ell|^\beta=0.68\psi_\infty/b_{cx}|\tau|^\beta. \tag{B12}$$

From Eq. (2.2), we have $q=\pm0.68$ on CX. In Fig. 18 we plot trajectories (t_ℓ,s_ℓ) (which are curves of constant q) and $\Delta(t_\ell,s_\ell)/[\Delta_{cri}+1.4|t_\ell|^{2\nu}]$ for several $(\hat{t},\hat{s})$. As stated below Eq. (B7), $\Delta(t_\ell,s_\ell)$ behaves near CX as

$$\Delta(t_\ell,s_\ell)\cong1.4|t_\ell|^{2\nu}\sim(\ell/\xi)^2, \tag{B13}$$

which indeed leads to Eq. (4.3) with the aid of Eq. (B8).

We further remark the following. (1) First, since $\Delta(t,s)\cong\Delta_{cri}$ for small t and s, $\mathcal{G}$ and $\mathcal{F}$ grow as in Eq. (3.27) for $\hat{\ell}\ll1$. (2) Second, for $\tau=0$ (at $T=T_c$), we obtain

$$\hat{\ell}^2\mathcal{F}(\hat{\ell})/\pi\cong\Delta(0,s_\ell). \tag{B14}$$

See Fig. 4 of Ref. [30] for $\Delta(0,s)$. For $\hat{s}>0$, $\hat{\ell}^2\mathcal{F}/\pi$ decays from Δ_{cri} to zero monotonously with increasing $\hat{\ell}$. For $\hat{s}<0$, it takes a large maximum about $3.73=13.4\Delta_{cri}$ at $s_\ell=-0.90$ or at

$$\hat{\ell}=0.82|\hat{s}|^{-\nu/\beta}=6.14\xi/a, \tag{B15}$$

where ξ is defined by Eq. (2.9) [see the discussion below Eq. (3.13)]. This explains the large maximum of $\hat{\ell}^2\mathcal{F}$ for $(\hat{t},\hat{s})=(0,-1)$ in Fig. 3. (3) Third, for $\psi_\infty=0$ and $\tau>0$ (on the critical path), we obtain

$$\hat{\ell}^2\mathcal{F}(\hat{\ell})/\pi\cong\Delta(t_\ell,0). \tag{B16}$$

See Fig. 8 of Ref. [30] for $\Delta(t,0)$. For $\hat{t}>0$, $\hat{\ell}^2\mathcal{F}/\pi$ starts from Δ_{cri}, takes a mild maximum about $0.544=1.95\Delta_{cri}$ at $t_\ell=2.30$ or at

$$\hat{\ell}\cong1.64\hat{t}^{-\nu}=1.64\xi/a, \tag{B17}$$

and goes to zero for larger $\hat{\ell}$. This yields the mild minimum of $\hat{\ell}^2\mathcal{F}$ for $(\hat{t},\hat{s})=(5,0)$ in Fig. 3.

We also discuss how $\mathcal{F}$ and $\mathcal{G}$ behave as functions of ℓ away from the criticality in separated states. Our previous work [30] indicates that if $|t|\gg1$ or $|s|\gg1$, $\mathcal{A}(t,s)$ for a film decays as

$$\mathcal{A}(t,s)\sim(D/\xi)^3\exp(-D/\xi), \tag{B18}$$

where ξ is defined by Eq. (2.9). This relation holds for $\psi_m\cong\psi_\infty$, which leads to $-\ln(\psi_m/\psi_\infty-1)\sim D/2\xi$ and $\mathcal{A}\cong D^3f''(\psi_\infty)(\psi_m-\psi_\infty)^2/k_BT_c$ [30]. In Eq. (B18), we next need to replace (t,s) by (t_ℓ,s_ℓ). To this end, we write ξ in the scaling form $\xi=\xi_0|\tau|^{-\nu}M(q)$ using q in Eq. (B12), where $M(q)$ is a scaling function of q. Then $D/\xi=|t|^\nu M(q)^{-1}$. Replacement of $(t,s)\to(t_\ell,s_\ell)$ yields $D/\xi\to|t_\ell|^\nu M(q)^{-1}=\ell/\xi$ so that

$$\mathcal{A}(t_\ell,s_\ell)\sim(\ell/\xi)^3\exp(-\ell/\xi). \tag{B19}$$

Substitution of this relation into Eq. (B11) and use of Eq. (3.24) give $\mathcal{F}$ and $\mathcal{G}$ in Eq. (3.28).

[1] R. Evans, J. Phys.: Condens. Matter **2**, 8989 (1990).
[2] L. D. Gelb, K. E. Gubbins, R. Radhakrishnan, and M. Sliwinska-Bartkowiak, Rep. Prog. Phys. **62**, 1573 (1999).
[3] J. N. Israelachvili, *Intermolecular and Surface Forces* (Academic Press, London, 1991).
[4] H.-J. Butt and M. Kappl, *Surface and Interfacial Forces* (Wiley-VCH, Weinheim, 2010).
[5] J. Dzubiella and J.-P. Hansen, J. Chem. Phys. **121**, 5514 (2004).
[6] P. Hopkins, A. J. Archer, and R. Evans, J. Chem. Phys. **131**, 124704 (2009).
[7] D. Beysens and D. Estève, Phys. Rev. Lett. **54**, 2123 (1985); D. Beysens, J.-M. Petit, T. Narayan, A. Kumar, and M. L. Broide, Ber. Bunsen-Ges. Phys. Chem. **98**, 382 (1994); B. M. Law, J.-M. Petit, and D. Beysens, Phys. Rev. E **57**, 5782 (1998); D. Beysens and T. Narayanan, J. Stat. Phys. **95**, 997 (1999).
[8] P. D. Gallagher and J. V. Maher, Phys. Rev. A **46**, 2012 (1992); P. D. Gallagher, M. L. Kurnaz, and J. V. Maher, *ibid.* **46**, 7750 (1992); M. L. Kurnaz and J. V. Maher, Phys. Rev. E **51**, 5916 (1995).
[9] H. Guo, T. Narayanan, M. Sztucki, P. Schall, and G. H. Wegdam, Phys. Rev. Lett. **100**, 188303 (2008).
[10] D. Bonn, J. Otwinowski, S. Sacanna, H. Guo, G. Wegdam, and P. Schall, Phys. Rev. Lett. **103**, 156101 (2009).
[11] T. J. Sluckin, Phys. Rev. A **41**, 960 (1990).

[12] H. Löwen, Phys. Rev. Lett. **74**, 1028 (1995).

[13] R. R. Netz, Phys. Rev. Lett. **76**, 3646 (1996).

[14] A. Hanke, F. Schlesener, E. Eisenriegler, and S. Dietrich, Phys. Rev. Lett. **81**, 1885 (1998).

[15] Y. Jayalakshmi and E. W. Kaler, Phys. Rev. Lett. **78**, 1379 (1997).

[16] R. Okamoto and A. Onuki, Phys. Rev. E **82**, 051501 (2010); A. Onuki, R. Okamoto, and T. Araki, Bull. Chem. Soc. Jpn. **84**, 569 (2011).

[17] C. Hertlein, L. Helden, A. Gambassi, S. Dietrich, and C. Bechinger, Nature (London) **451**, 172 (2008).

[18] U. Nellen, L. Helden, and C. Bechinger, Europhys. Lett. **88**, 26001 (2009); U. Nellen, J. Dietrich, L. Helden, S. Chodankar, K. Nygaard, J. F. van der Veen, and C. Bechinger, Soft Matter **7**, 5360 (2011).

[19] W. B. Russel, D. A. Saville, and W. R. Schowalter, *Colloidal Dispersions* (Cambridge University Press, Cambridge, 1989).

[20] D. Bonn and D. Ross, Rep. Prog. Phys. **64**, 1085 (2001).

[21] D. Dantchev, F. Schlesener, and S. Dietrich, Phys. Rev. E **76**, 011121 (2007).

[22] R. Okamoto and A. Onuki, Phys. Rev. E **84**, 051401 (2011).

[23] M. E. Fisher and P. G. de Gennes, C. R. Acad. Sci. Paris Ser. **287**, 207 (1978).

[24] M. E. Fisher and H. Au-Yamg, Physica A **101**, 255 (1980); M. E. Fisher and P. J. Upton, Phys. Rev. Lett. **65**, 3405 (1990).

[25] Z. Borjan and P. J. Upton, Phys. Rev. Lett. **81**, 4911 (1998); **101**, 125702 (2008).

[26] A. Gambassi, A. Maciołek, C. Hertlein, U. Nellen, L. Helden, C. Bechinger, and S. Dietrich, Phys. Rev. E **80**, 061143 (2009); A. Gambassi and S. Dietrich, Phys. Rev. Lett. **105**, 059601 (2010).

[27] A. Mukhopadhyay and B. M. Law, Phys. Rev. E **63**, 041605 (2001); M. Fukuto, Y. F. Yano, and P. S. Pershan, Phys. Rev. Lett. **94**, 135702 (2005); S. Rafai, D. Bonn, and J. Meunier, Physica A **386**, 31 (2007).

[28] The Casimir interaction was originally found to be induced by the ground-state fluctuations of the electromagnetic field between two mirrors. In near-critical fluids, the solvent-mediated interaction is caused by preferential adsorption, where the composition heterogeneity is stationary for fixed colloid positions. From our viewpoint, it is misleading to call it the Casimir interaction, Thus we call it the adsorption-induced interaction [7].

[29] A. Maciołek, A. Drzewiński, and R. Evans, Phys. Rev. E **64**, 056137 (2001).

[30] R. Okamoto and A. Onuki, J. Chem. Phys. **136**, 114704 (2012).

[31] S. Yabunaka, R. Okamoto, and A. Onuki, Phys. Rev. E **87**, 032405 (2013).

[32] H.-J. Butt and M. Kappl, Adv. Colloid Interf. Sci. **146**, 48 (2009).

[33] H. T. Dobbs, G. A. Darbellay, and J. M. Yeomans, Europhys. Lett. **18**, 439 (1992); H. T. Dobbs and J. M. Yeomans, J. Phys.: Condens. Matter **4**, 10133 (1992).

[34] D. Andrienko, P. Patricio, and O. I. Vinogradova, J. Chem. Phys. **121**, 4414 (2004).

[35] C. Bauer, T. Bieker, and S. Dietrich, Phys. Rev. E **62**, 5324 (2000).

[36] H. Shinto, K. Uranishi, H. Miyahara, and K. Higashitani, J. Chem. Phys. **116**, 9500 (2002).

[37] A. Carambassis, L. C. Jonker, P. Attard, and M. W. Rutland, Phys. Rev. Lett. **80**, 5357 (1998); G. E. Yakubov, H. J. Butt, and O. I. Vinogradova, J. Phys. Chem. B **104**, 3407 (2000).

[38] R. Teshigawara and A. Onuki, Phys. Rev. E **84**, 041602 (2011).

[39] K. Kocevar, A. Borstnik, I. Musevic, and S. Zumer, Phys. Rev. Lett. **86**, 5914 (2001).

[40] H. Stark, J. I. Fukuda, and H. Yokoyama, Phys. Rev. Lett. **92**, 205502 (2004).

[41] P. Schofield, Phys. Rev. Lett. **22**, 606 (1969); P. Schofield, J. D. Lister, and J. T. Ho, *ibid.* **23**, 1098 (1969).

[42] A. Onuki, *Phase Transition Dynamics* (Cambridge University Press, Cambridge, 2002).

[43] The coefficient C_1 in Ref. [30] is set equal to 1 in the present paper. Then C is dimensionless.

[44] J. Rudnick and D. Jasnow, Phys. Rev. Lett. **48**, 1059 (1982); **49**, 1595 (1982).

[45] R. Holyst and A. Poniewierski, Phys. Rev. B **36**, 5628 (1987); M. P. Gefand and R. Lipowsky, *ibid.* **36**, 8725 (1987); P. J. Upton, J. O. Indekeu, and J. M. Yeomans, *ibid.* **40**, 666 (1989).

[46] In the weak adsorption regime, we have $\Delta F_{\rm sol}/4\pi a^2 \cong 2k_BT_ch_1\psi_{\rm cx} \propto |\tau|^\beta$. If $h_1 \ll \xi_0^{-3/2}$, this holds even relatively close to the criticality. For $h_1 > \xi_0^{-3/2}|\tau|^{2\nu-\beta}$, however, $\Delta F_{\rm sol}/4\pi a^2$ becomes about σ as in Eq. (3.20).

[47] W. Schmickler, *Interfacial Electrochemistry* (Oxford University Press, Oxford, 1996).

[48] For $\tau = 0$, ψ and $\omega_{\rm loc}$ are calculated as $\psi_m = 0.7107\psi_D$ and $\omega_m = 0.205k_BT_cD^{-3}$, respectively, at $z = D/2$ in the film geometry [30]. See Eq. (B3) for ψ_D.

[49] The authors of Ref. [26] obtained $\mathcal{G} = \pi Aa\xi^{-1}\exp(-\ell/\xi)$ with $A = 1.2 - 1.4$ for $\ell > \xi$ on the critical path ($\tau > 0$ and $\psi_\infty = 0$). In our scheme, the curve of $\ln(\mathcal{G})$ for $(\hat{t},\hat{s}) = (5,0)$ in Fig. 6 gives $A \cong 0.9$ on the critical path.

[50] J.-M. Petit, B. M. Law, and D. Beysens, J. Colloid Interf. Sci. **202**, 441 (1998).

[51] K. Takahashi, M. Ichikawa, and Y. Kimura, Phys. Rev. E **77**, 020703(R) (2008).

[52] For small $s + s_{\rm cx}$ (near CX) and for $|t| \gg 1$, we have $\psi_m \cong \psi_{\rm cx}$ (see Fig. 6 of Ref. [30]). Then, $\mathcal{A} \cong A_0|t|^{3\nu}[-(s/s_{\rm cx}+1) + A_1e^{-D/\xi}]$ where $A_0 \cong 0.078$ and $A_1 \cong 0.56$.